

Non-oscillatory Central Schemes for Hyperbolic Systems of Conservation Laws in Three Space Dimensions

*Abhilash J. Chandy¹, and Steven H. Frankel²

¹ *Department of Mechanical Engineering, University of Akron, Akron, OH*

44325-3903

² *School of Mechanical Engineering, Purdue University, West Lafayette, IN*

47907-2088

Abstract

We extend a family of high-resolution, semi-discrete central schemes for hyperbolic systems of conservation laws to three space dimensions. Details of the schemes, their implementation, and properties are presented together with results from several prototypical applications of hyperbolic conservation laws including a non-linear scalar equation, the Euler equations of gas dynamics, and the ideal magnetohydrodynamic equations. Parallel scaling analysis and grid-independent results including contours and isosurfaces of density, and velocity and magnetic field vectors are shown in this study, confirming the ability of these type of solvers to approximate the solutions of hyperbolic equations efficiently and accurately.

*Corresponding author: Email: achandy@uakron.edu (Abhilash Chandy)

1 Introduction

Over the past couple decades, much work has gone into the construction, analysis, and implementation of modern numerical algorithms for the approximate solution of systems of nonlinear hyperbolic conservation laws of the form:

$$(u)_t + f(u)_x + g(u)_y + h(u)_z = 0. \quad (1)$$

Numerical solutions of these equations are of tremendous practical importance as they govern a variety of physical phenomena in natural and engineering applications, including astrophysical, geophysical, and thermochemical fluid flows. A number of high-resolution schemes were developed and tested for this purpose [1–6]. The first-order Lax-Friedrichs scheme [7] is actually the forerunner for a large class of central high-resolution schemes that have seen much development in recent years. One of the main differences between high-resolution schemes and other methods, e.g. Godunov or upwind methods, is that instead of using a single cell average (which contains relatively little information), neighboring cell averages are used to reconstruct an approximate polynomial solution within each cell. This paper presents the formulation and testing of such $3D$ high resolution semi-discrete schemes developed first by Nessyahu and Tadmor [2].

The paper is organized as follows: In section 2 we briefly describe the background with regard to the development of semi-discrete central schemes. This is followed by the mathematical formulation in sections 3 and 4. Section 5 presents a set of three $3D$ test cases and their results obtained using the semi-discrete schemes formulated in this paper, including a parallel scaling analysis. Section 6 summarizes the entire study.

2 Background

The focus of this paper is on central schemes, all of which can be viewed as an extension of the well-known Lax-Friedrichs scheme [7]. The first-order Lax-Friedrichs scheme enjoys a major advantage of simplicity over most upwind schemes, in that no approximate Riemann solvers or characteristic decompositions are involved in its construction, thereby offering a rather simple realization for complicated multidimensional systems. However, the Lax-Friedrichs scheme suffers from excessive numerical dissipation, resulting in poor resolution of discontinuities and rarefaction waves. To circumvent this deficiency, Nessyahu and Tadmor introduced a second-order non-oscillatory central scheme (NT scheme) in 1990, [2], which was further extended to higher orders of accuracy [8–10], as well as to multidimensional systems [11,12,3].

The main ingredient in the construction of the NT method is a second-order non-oscillatory, monotonic upstream scheme for conservation laws (MUSCL)-type [13], piecewise linear interpolant (instead of the piecewise constant one employed in the Lax-Friedrichs scheme) in combination with an higher-order solver for the time evolution [4]. However, applying the fully discrete NT scheme to the second-order convection-diffusion equations still does not provide the desired resolution of discontinuities (see [14–16]). This loss of resolution occurs due to the accumulation of excessive numerical dissipation, which is typical of fully discrete schemes with small time steps since $\Delta t \propto (\Delta x)^2$ [4,16]. This led Kurganov and Tadmor [16] to the development of a set of second-order semi-discrete central schemes. These schemes have smaller dissipation than the original NT scheme and, unlike the fully discrete central schemes, they can be efficiently used with time steps as small as required by

the CFL stability restriction due to the diffusion term.

In the study of Kurganov and Tadmor [16], a non-staggered semidiscrete central method was derived by first integrating over non-equally spaced volumes, out of which a new piecewise linear interpolant was reconstructed and finally projected on its cell-averages [17]. The schemes in [16] were further extended to third-order in [4], where a new central weighted essentially non-oscillatory (CWENO) reconstruction, originally proposed in [3], was used to provide a third-order accurate interpolant, built from the given cell-averages such that it is non-oscillatory in the essentially non-oscillatory (ENO) sense [18,19]. Such weighted essentially non-oscillatory (WENO) reconstructions were introduced first in an upwind framework [20], after which they were extended to a central framework [9,12,3]

More recently Balbas and Tadmor [21,6] presented extensions of the semidiscrete central schemes of [16] with arbitrary order, r , specifically third- and fourth-order reconstructions with the possibility of additional reconstructions in the diagonal directions. While the schemes in [21,6] were presented for two-dimensional systems, a $3D$ formulation of such semidiscrete central schemes has not been published to the best of the authors' knowledge. In this paper, we present and test the third-order accurate semidiscrete central schemes of Balbas and Tadmor [6] for $3D$ systems of equations.

3 Formulation

3.1 Governing equations

In this paper, we present third-order accurate, non-oscillatory semi-discrete central schemes for the approximate solution of several hyperbolic conservation laws, including the single non-linear scalar equation given by

$$(u)_t + (u^2)_x + (u^2)_y + (u^2)_z = 0, \quad (2)$$

Euler equations of gas dynamics given by

$$(\rho)_t + \nabla \cdot (\rho \mathbf{v}) = 0 \quad (3)$$

$$(\rho \mathbf{v})_t + \nabla \cdot [(\rho \mathbf{v} \mathbf{v}^T) + p \mathbf{I}] = 0 \quad (4)$$

$$(E)_t + \nabla \cdot \left[\left(\frac{\gamma}{\gamma - 1} p + \frac{1}{2} \rho v^2 \right) \mathbf{v} \right] = 0 \quad (5)$$

and the system of equations for ideal magnetohydrodynamics (MHD) given by

$$(\rho)_t + \nabla \cdot (\rho \mathbf{v}) = 0 \quad (6)$$

$$(\rho \mathbf{v})_t + \nabla \cdot \left[(\rho \mathbf{v} \mathbf{v}^T) + \left(p + \frac{1}{2} B^2 \right) \mathbf{I} - \mathbf{B} \mathbf{B}^T \right] = 0 \quad (7)$$

$$(\mathbf{B})_t - \nabla \times (\mathbf{v} \times \mathbf{B}) = 0 \quad (8)$$

$$(E)_t + \nabla \cdot \left[\left(\frac{\gamma}{\gamma - 1} p + \frac{1}{2} \rho v^2 \right) \mathbf{v} - (\mathbf{v} \times \mathbf{B}) \times \mathbf{B} \right] = 0 \quad (9)$$

Here ρ and E are scalar quantities representing the mass density and total internal energy, respectively, $\mathbf{v} = (u, v, w)^T$ is the velocity field with *Euclidean* norm $v^2 := \|\mathbf{v}\|^2$, and $\mathbf{B} = (B_1, B_2, B_3)^T$ and $B^2 := \|\mathbf{B}\|^2$ represent the magnetic field and its norm, respectively. The pressure, p , is coupled to the total internal energy, $E = \frac{1}{2} \rho v^2 + p/(\gamma - 1) + \frac{1}{2} B^2$ ($\mathbf{B} = 0$ in (3)-(5)). Furthermore, the system of MHD equations ((6)-(9)) is augmented by the solenoidal

constraint, that is, if the condition $\nabla \cdot \mathbf{B} = 0$ is satisfied initially at $t = 0$, then by (8) it remains invariant in time.

3.2 Third-order semi-discrete schemes

Starting with a general hyperbolic conservation law in three-space dimensions,

$$(u)_t + f(u)_x + g(u)_y + h(u)_z = 0, \quad (10)$$

let the sliding averages of u over the cells $C_{i,j,k} := [x_{i-1/2}, x_{i+1/2}] \times [y_{j-1/2}, y_{j+1/2}] \times [z_{k-1/2}, z_{k+1/2}]$ (see Fig. 1) at time level, n , be

$$\bar{u}_{i,j,k}^n := \int_{C_{i,j,k}} u(x, y, z, t^n) dx dy dz, \quad (11)$$

where dx, dy and dz are the cell widths in the x -, y - and z -directions, respectively. The local speeds of wave propagation are approximated by

$$\begin{aligned} a_{i+\frac{1}{2},j,k}^n &:= \max \left[\rho \left(\frac{\partial f}{\partial u}(u_{i+1,j,k}^{LC}) \right), \rho \left(\frac{\partial f}{\partial u}(u_{i,j,k}^{RC}) \right) \right], \\ b_{i,j+\frac{1}{2},k}^n &:= \max \left[\rho \left(\frac{\partial g}{\partial u}(u_{i,j+1,k}^{BC}) \right), \rho \left(\frac{\partial g}{\partial u}(u_{i,j,k}^{TC}) \right) \right], \\ c_{i,j,k+\frac{1}{2}}^n &:= \max \left[\rho \left(\frac{\partial h}{\partial u}(u_{i,j,k+1}^{BaC}) \right), \rho \left(\frac{\partial h}{\partial u}(u_{i,j,k}^{FC}) \right) \right]; \end{aligned} \quad (12)$$

where the supercripts LC, RC, BC, TC, BaC and FC stand for the **L**eft, **R**ight, **B**ottom, **T**op, **B**ack and **F**ront **C**enters respectively (Fig. 2). The cell

interface values in the x -, y -, and z -directions,

$$\begin{aligned}
u_{i,j,k}^{RC} &:= p_{i,j,k}^n(x_{i+\frac{1}{2}}, y_j, z_k), \\
u_{i,j,k}^{LC} &:= p_{i,j,k}^n(x_{i-\frac{1}{2}}, y_j, z_k), \\
u_{i,j,k}^{TC} &:= p_{i,j,k}^n(x_i, y_{j+\frac{1}{2}}, z_k), \\
u_{i,j,k}^{BC} &:= p_{i,j,k}^n(x_i, y_{j-\frac{1}{2}}, z_k), \\
u_{i,j,k}^{FC} &:= p_{i,j,k}^n(x_i, y_j, z_{k+\frac{1}{2}}), \\
u_{i,j,k}^{BaC} &:= p_{i,j,k}^n(x_i, y_j, z_{k-\frac{1}{2}}).
\end{aligned} \tag{13}$$

are calculated via a non-oscillatory piecewise polynomial reconstruction,

$$R(x, y, z; \bar{u}^n) = \sum_{i,j,k} p_{i,j,k}^n(x, y, z) \mathbf{1}_{C_{i,j,k}}; \tag{14}$$

Details about the derivation of the polynomials and their properties can be found in [6].

The resulting semi-discrete scheme in the limit as $\Delta \rightarrow 0$ is as follows:

$$\begin{aligned}
\frac{d}{dt} \bar{u}_{i,j,k}(t) = & - \frac{H_{i+\frac{1}{2},j,k}^x(t) - H_{i-\frac{1}{2},j,k}^x(t)}{\Delta x} - \frac{H_{i,j+\frac{1}{2},k}^y(t) - H_{i,j-\frac{1}{2},k}^y(t)}{\Delta y} \\
& - \frac{H_{i,j,k+\frac{1}{2}}^z(t) - H_{i,j,k-\frac{1}{2}}^z(t)}{\Delta z} \tag{15}
\end{aligned}$$

with numerical fluxes

$$\begin{aligned}
H_{i+\frac{1}{2},j,k}^x(t) &= \frac{1}{2} [f(u_{i+1,j,k}^{LC}) + f(u_{i,j,k}^{RC})] - \frac{a_{i+\frac{1}{2},j,k}(t)}{2} [u_{i+1,j,k}^{LC} + u_{i,j,k}^{RC}] \\
H_{i,j+\frac{1}{2},k}^y(t) &= \frac{1}{2} [g(u_{i,j+1,k}^{TC}) + g(u_{i,j,k}^{BC})] - \frac{b_{i,j+\frac{1}{2},k}(t)}{2} [u_{i,j+1,k}^{TC} + u_{i,j,k}^{BC}] \\
H_{i,j,k+\frac{1}{2}}^z(t) &= \frac{1}{2} [h(u_{i,j,k+1}^{FC}) + h(u_{i,j,k}^{BaC})] - \frac{c_{i,j,k+\frac{1}{2}}(t)}{2} [u_{i,j,k+1}^{FC} + u_{i,j,k}^{BaC}]
\end{aligned} \tag{16}$$

for the third-order CWENO reconstruction without any diagonal smoothing (diagonal smoothing described in the next section). If diagonal smoothing is

to be applied, the numerical fluxes are given by,

$$\begin{aligned}
H_{i+\frac{1}{2},j,k}^x(t) &= \frac{1}{24} \left[f(u_{i+1,j,k}^{LTF}) + f(u_{i,j,k}^{RTF}) + 4 \left(f(u_{i+1,j,k}^{LTBa}) + f(u_{i,j,k}^{RTBa}) \right) \right. \\
&+ 2 \left(f(u_{i+1,j,k}^{LC}) + f(u_{i,j,k}^{RC}) \right) + 4 \left(f(u_{i+1,j,k}^{LTF}) + f(u_{i,j,k}^{RBF}) \right) + f(u_{i+1,j,k}^{LBBa}) + f(u_{i,j,k}^{RBBa}) \left. \right] \\
&\quad - \frac{a_{i+\frac{1}{2},j,k}(t)}{24} \left[u_{i+1,j,k}^{LTF} + u_{i,j,k}^{RTF} + 4 \left(u_{i+1,j,k}^{LTBa} + u_{i,j,k}^{RTBa} \right) + \right. \\
&\quad \left. 2 \left(u_{i+1,j,k}^{LC} + u_{i,j,k}^{RC} \right) + 4 \left(u_{i+1,j,k}^{LTF} + u_{i,j,k}^{RBF} \right) + u_{i+1,j,k}^{LBBa} + u_{i,j,k}^{RBBa} \right] \quad (17)
\end{aligned}$$

$$\begin{aligned}
H_{i,j+\frac{1}{2},k}^y(t) &= \frac{1}{24} \left[g(u_{i,j+1,k}^{LBBa}) + g(u_{i,j,k}^{LTBa}) + 4 \left(g(u_{i,j+1,k}^{LBF}) + g(u_{i,j,k}^{LTF}) \right) \right. \\
&+ 2 \left(g(u_{i,j+1,k}^{BC}) + g(u_{i,j,k}^{TC}) \right) + 4 \left(g(u_{i,j+1,k}^{RBBa}) + g(u_{i,j,k}^{RTBa}) \right) + g(u_{i,j+1,k}^{RBF}) + g(u_{i,j,k}^{RTF}) \left. \right] \\
&\quad - \frac{b_{i,j+\frac{1}{2},k}(t)}{24} \left[u_{i,j+1,k}^{LBBa} + u_{i,j,k}^{LTBa} + 4 \left(u_{i,j+1,k}^{LBF} + u_{i,j,k}^{LTF} \right) + \right. \\
&\quad \left. 2 \left(u_{i,j+1,k}^{BC} + u_{i,j,k}^{TC} \right) + 4 \left(u_{i,j+1,k}^{RBBa} + u_{i,j,k}^{RTBa} \right) + u_{i,j+1,k}^{RBF} + u_{i,j,k}^{RTF} \right] \quad (18)
\end{aligned}$$

$$\begin{aligned}
H_{i,j,k+\frac{1}{2}}^z(t) &= \frac{1}{24} \left[h(u_{i,j,k+1}^{RTBa}) + h(u_{i,j,k}^{RTF}) + 4 \left(h(u_{i,j,k+1}^{LTBa}) + h(u_{i,j,k}^{LTF}) \right) \right. \\
&+ 2 \left(h(u_{i,j,k+1}^{BaC}) + h(u_{i,j,k}^{FC}) \right) + 4 \left(h(u_{i,j,k+1}^{RBBa}) + h(u_{i,j,k}^{RBF}) \right) + h(u_{i,j,k+1}^{LBBa}) + h(u_{i,j,k}^{LBF}) \left. \right] \\
&\quad - \frac{c_{i,j,k+\frac{1}{2}}(t)}{24} \left[u_{i,j,k+1}^{RTBa} + u_{i,j,k}^{RTF} + 4 \left(u_{i,j,k+1}^{LTBa} + u_{i,j,k}^{LTF} \right) + \right. \\
&\quad \left. 2 \left(u_{i,j,k+1}^{BaC} + u_{i,j,k}^{FC} \right) + 4 \left(u_{i,j,k+1}^{RBBa} + u_{i,j,k}^{RBF} \right) + u_{i,j,k+1}^{LBBa} + u_{i,j,k}^{LBF} \right] \quad (19)
\end{aligned}$$

where the superscripts *RTF*, *LBBa*, *RBF*, *LTBa*, *LTF*, *RBBa*, *LBF*, and *RTBa* stand for **Right-Top-Front**, **Left-Bottom-Back**, **Right-Bottom-Front**, **Left-Top-Back**, **Left-Top-Front**, **Right-Bottom-Back**, **Left-Bottom-Front**, and **Right-Top-Back**, respectively (Fig. 3).

This particular version of the numerical fluxes results from using Simpson's quadrature rule to approximate the intergrals of the fluxes f , g and h along

the cell boundaries $[x_{i-\frac{1}{2}}, x_{i+\frac{1}{2}}]$, $[y_{j-\frac{1}{2}}, y_{j+\frac{1}{2}}]$ and $[z_{k-\frac{1}{2}}, z_{k+\frac{1}{2}}]$, respectively, and it incorporates information from the corner interface values,

$$\begin{aligned}
u_{i,j,k}^{RTF} &:= \hat{p}_{i,j,k}^n \left(x_{i+\frac{1}{2}}, y_{j+\frac{1}{2}}, z_{k+\frac{1}{2}} \right) \\
u_{i,j,k}^{LBBa} &:= \hat{p}_{i,j,k}^n \left(x_{i-\frac{1}{2}}, y_{j-\frac{1}{2}}, z_{k-\frac{1}{2}} \right) \\
u_{i,j,k}^{RBF} &:= \hat{p}_{i,j,k}^n \left(x_{i+\frac{1}{2}}, y_{j-\frac{1}{2}}, z_{k+\frac{1}{2}} \right) \\
u_{i,j,k}^{LTBa} &:= \hat{p}_{i,j,k}^n \left(x_{i-\frac{1}{2}}, y_{j+\frac{1}{2}}, z_{k-\frac{1}{2}} \right) \\
u_{i,j,k}^{LTF} &:= \hat{p}_{i,j,k}^n \left(x_{i-\frac{1}{2}}, y_{j+\frac{1}{2}}, z_{k+\frac{1}{2}} \right) \\
u_{i,j,k}^{RBBa} &:= \hat{p}_{i,j,k}^n \left(x_{i+\frac{1}{2}}, y_{j-\frac{1}{2}}, z_{k-\frac{1}{2}} \right) \\
u_{i,j,k}^{LBF} &:= \hat{p}_{i,j,k}^n \left(x_{i-\frac{1}{2}}, y_{j-\frac{1}{2}}, z_{k+\frac{1}{2}} \right) \\
u_{i,j,k}^{RTBa} &:= \hat{p}_{i,j,k}^n \left(x_{i+\frac{1}{2}}, y_{j+\frac{1}{2}}, z_{k-\frac{1}{2}} \right)
\end{aligned} \tag{20}$$

into the scheme. These corner values are recovered again via a non-oscillatory reconstruction.

4 Implementation of Semi-Discrete Central Schemes

This section provides a third-order non-oscillatory reconstruction in three-space dimensions, that was implemented for computing the solutions of (2), (3) - (5) and (6) - (9).

4.1 Corner Reconstructions

The reconstruction of the point values of u presented in this section is the third-order CWENO polynomial reconstruction of Kurganov and Levy [4]. The properties of the piecewise quadratic polynomial, that is used here, were presented in [4] and [6]. In each cell $C_{i,j,k} = [x_{i-\frac{1}{2}}, x_{i+\frac{1}{2}}] \times [y_{j-\frac{1}{2}}, y_{j+\frac{1}{2}}] \times [z_{k-\frac{1}{2}}, z_{k+\frac{1}{2}}]$,

the polynomials $[p_{i,j,k}^n(x, y, z)]$ in Eqns. (13) and (20) are written as a convex combination of three polynomials $P_{-1}(x, y, z)$, $P_0(x, y, z)$, and $P_1(x, y, z)$. In the x -direction they are as follows:

$$p_{i,j,k}^n(x, y, z) = w_{-1}P_{-1}(x, y, z) + w_0P_0(x, y, z) + w_1P_1(x, y, z), \quad (21)$$

$$\sum_{m \in \{-1, 0, 1\}} w_m = 1$$

where the linear polynomials

$$P_{-1}(x, y, z) = \bar{u}_{i,j,k}^n + \frac{\bar{u}_{i,j,k}^n - \bar{u}_{i-1,j,k}^n}{\Delta x}(x - x_i), \quad (22)$$

and

$$P_1(x, y, z) = \bar{u}_{i,j,k}^n + \frac{\bar{u}_{i+1,j,k}^n - \bar{u}_{i,j,k}^n}{\Delta x}(x - x_i) \quad (23)$$

conserve the pair of cell averages $\bar{u}_{i-1,j,k}^n, \bar{u}_{i,j,k}^n$ and $\bar{u}_{i,j,k}^n, \bar{u}_{i+1,j,k}^n$, respectively, and the parabola centered around x_i is given by,

$$P_0(x, y, z) = \bar{u}_{i,j,k}^n - \frac{1}{12} \left(\bar{u}_{i-1,j,k}^n + \bar{u}_{i+1,j,k}^n - 6\bar{u}_{i,j,k}^n + \bar{u}_{i,j-1,k}^n + \bar{u}_{i,j+1,k}^n + \bar{u}_{i,j,k-1}^n + \bar{u}_{i,j,k+1}^n \right) + \frac{\bar{u}_{i+1,j,k}^n - \bar{u}_{i-1,j,k}^n}{2\Delta x}(x - x_i) + \frac{\bar{u}_{i+1,j,k}^n - \bar{u}_{i,j,k}^n + \bar{u}_{i-1,j,k}^n}{\Delta x^2}(x - x_i)^2. \quad (24)$$

The conservation of the cell averages $\bar{u}_{i-1,j,k}^n, \bar{u}_{i,j,k}^n, \bar{u}_{i+1,j,k}^n$ and the accuracy property (property **P₂** in [6]) are guaranteed [6] by any symmetric choice of weights c_m (e.g., $c_{-1} = c_1 = 1/4, c_0 = 1/2$). The non-oscillatory behavior (property **P₃** in [6]) is attained with non-linear weights

$$w_m = \frac{\alpha_m}{\sum_l \alpha_l}, \quad \text{with} \quad \alpha_m = \frac{c_m}{(\epsilon + IS_m)^2}, \quad m, l \in \{-1, 0, 1\} \quad (25)$$

$\epsilon \ll 1$ prevents the denominator from being zero ($\epsilon = 10^{-6}$), and the smoothness indicators provide a local measure of the derivatives $P_m(x, y, z)$, and in

this case they read

$$\begin{aligned}
IS_{-1} &= (\bar{u}_{i,j,k}^n - \bar{u}_{i-1,j,k}^n)^2 \\
IS_1 &= (\bar{u}_{i+1,j,k}^n - \bar{u}_{i,j,k}^n)^2 \\
IS_0 &= \frac{13}{3}(\bar{u}_{i+1,j,k}^n - 2\bar{u}_{i,j,k}^n + \bar{u}_{i-1,j,k}^n)^2 + \frac{1}{4}(\bar{u}_{i+1,j,k}^n - \bar{u}_{i-1,j,k}^n)^2
\end{aligned} \tag{26}$$

In the case of systems of equations, the smoothness indicators are given by the *norm-scaled* average of the componentwise indicators, $IS_m^{(nq)}$, given by

$$IS_m = \frac{1}{EQ} \sum_{nq=1}^{EQ} \frac{1}{\|u^{(nq)}\|_2 + \epsilon} IS_m^{(nq)}, \quad m \in \{-1, 0, 1\}, \tag{27}$$

where $u^{(nq)}$ stands for the $(nq)^{th}$ component of u , and

$$\|u^{(nq)}\|_2 = \sum_{i,j,k} |u_{i,j,k}^{(nq)}|^2 \Delta x \Delta y \Delta z \tag{28}$$

represents its l_2 norm over the discretized solution domain.

The interface values are now given by

$$\begin{aligned}
u_{i,j,k}^{RC} &= w_{-1} \left[\bar{u}_{i,j,k}^n + \frac{1}{2}(\bar{u}_{i,j,k}^n - \bar{u}_{i-1,j,k}^n) \right] + w_0 \left[\bar{u}_{i,j,k}^n \right. \\
&\quad - \frac{1}{12}(\bar{u}_{i-1,j,k}^n + \bar{u}_{i+1,j,k}^n - 6\bar{u}_{i,j,k}^n + \bar{u}_{i,j-1,k}^n + \bar{u}_{i,j+1,k}^n + \bar{u}_{i,j,k-1}^n + \bar{u}_{i,j,k+1}^n) \\
&\quad \left. + \frac{1}{2}(\bar{u}_{i+1,j,k}^n - \bar{u}_{i-1,j,k}^n) + \frac{1}{4}(\bar{u}_{i+1,j,k}^n - \bar{u}_{i,j,k}^n + \bar{u}_{i-1,j,k}^n) \right] \\
&\quad + w_1 \left[\bar{u}_{i,j,k}^n + \frac{1}{2}(\bar{u}_{i+1,j,k}^n - \bar{u}_{i,j,k}^n) \right] \tag{29}
\end{aligned}$$

and

$$\begin{aligned}
u_{i,j,k}^{LC} &= w_{-1} \left[\bar{u}_{i,j,k}^n - \frac{1}{2}(\bar{u}_{i,j,k}^n - \bar{u}_{i-1,j,k}^n) \right] + w_0 \left[\bar{u}_{i,j,k}^n \right. \\
&\quad - \frac{1}{12}(\bar{u}_{i-1,j,k}^n + \bar{u}_{i+1,j,k}^n - 6\bar{u}_{i,j,k}^n + \bar{u}_{i,j-1,k}^n + \bar{u}_{i,j+1,k}^n + \bar{u}_{i,j,k-1}^n + \bar{u}_{i,j,k+1}^n) \\
&\quad \left. - \frac{1}{2}(\bar{u}_{i+1,j,k}^n - \bar{u}_{i-1,j,k}^n) + \frac{1}{4}(\bar{u}_{i+1,j,k}^n - \bar{u}_{i,j,k}^n + \bar{u}_{i-1,j,k}^n) \right] \\
&\quad + w_1 \left[\bar{u}_{i,j,k}^n - \frac{1}{2}(\bar{u}_{i+1,j,k}^n - \bar{u}_{i,j,k}^n) \right] \tag{30}
\end{aligned}$$

Similar reconstructions can be carried out in the y - and z - directions and the interface values $u_{i,j,k}^{FC}$, $u_{i,j,k}^{BaC}$, $u_{i,j,k}^{TC}$ and $u_{i,j,k}^{BC}$ can be derived in a straightforward manner. For example, the interface values $u_{i,j,k}^{TC}$ and $u_{i,j,k}^{BC}$ will be given by

$$\begin{aligned}
u_{i,j,k}^{TC} = & w_{-1} \left[\bar{u}_{i,j,k}^n + \frac{1}{2} \left(\bar{u}_{i,j,k}^n - \bar{u}_{i,j-1,k}^n \right) \right] + w_0 \left[\bar{u}_{i,j,k}^n \right. \\
& - \frac{1}{12} \left(\bar{u}_{i,j-1,k}^n + \bar{u}_{i,j+1,k}^n - 6\bar{u}_{i,j,k}^n + \bar{u}_{i-1,j,k}^n + \bar{u}_{i+1,j,k}^n + \bar{u}_{i,j,k-1}^n + \bar{u}_{i,j,k+1}^n \right) \\
& \left. + \frac{1}{2} \left(\bar{u}_{i,j+1,k}^n - \bar{u}_{i,j-1,k}^n \right) + \frac{1}{4} \left(\bar{u}_{i,j+1,k}^n - \bar{u}_{i,j,k}^n + \bar{u}_{i,j-1,k}^n \right) \right] \\
& + w_1 \left[\bar{u}_{i,j,k}^n + \frac{1}{2} \left(\bar{u}_{i,j+1,k}^n - \bar{u}_{i,j,k}^n \right) \right] \quad (31)
\end{aligned}$$

and

$$\begin{aligned}
u_{i,j,k}^{BC} = & w_{-1} \left[\bar{u}_{i,j,k}^n - \frac{1}{2} \left(\bar{u}_{i,j,k}^n - \bar{u}_{i,j-1,k}^n \right) \right] + w_0 \left[\bar{u}_{i,j,k}^n \right. \\
& - \frac{1}{12} \left(\bar{u}_{i,j-1,k}^n + \bar{u}_{i,j+1,k}^n - 6\bar{u}_{i,j,k}^n + \bar{u}_{i-1,j,k}^n + \bar{u}_{i+1,j,k}^n + \bar{u}_{i,j,k-1}^n + \bar{u}_{i,j,k+1}^n \right) \\
& - \frac{1}{2} \left(\bar{u}_{i,j+1,k}^n - \bar{u}_{i,j-1,k}^n \right) + \frac{1}{4} \left(\bar{u}_{i,j+1,k}^n - \bar{u}_{i,j,k}^n + \bar{u}_{i,j-1,k}^n \right) \left. \right] \\
& + w_1 \left[\bar{u}_{i,j,k}^n - \frac{1}{2} \left(\bar{u}_{i,j+1,k}^n - \bar{u}_{i,j,k}^n \right) \right] \quad (32)
\end{aligned}$$

4.2 Diagonal Reconstructions

Furthermore, if reconstructions are implemented along the diagonal directions (Fig. 3), then the corresponding polynomials are given by ([22])

$$\hat{p}_{i,j,k}^n(x, y, z) = \hat{w}_{-1} \hat{P}_{-1}(x, y, z) + \hat{w}_0 \hat{P}_0(x, y, z) + \hat{w}_1 \hat{P}_1(x, y, z) \quad (33)$$

where the linear polynomials are given by

$$\begin{aligned}
\hat{P}_{-1}(x, y, z) = & \bar{u}_{i,j,k}^n + \\
& \frac{\bar{u}_{i,j,k}^n - \bar{u}_{i-1,j-1,k-1}^n}{\Delta} \left(\frac{\Delta}{2\Delta x} (x - x_i) + \frac{\Delta}{2\Delta y} (y - y_j) + \frac{\Delta}{2\Delta z} (z - z_k) \right), \quad (34)
\end{aligned}$$

$$\hat{P}_1(x, y, z) = \bar{u}_{i,j,k}^n + \frac{\bar{u}_{i+1,j+1,k+1}^n - \bar{u}_{i,j,k}^n}{\Delta} \left(\frac{\Delta}{2\Delta x}(x - x_i) + \frac{\Delta}{2\Delta y}(y - y_j) + \frac{\Delta}{2\Delta z}(z - z_k) \right), \quad (35)$$

and

$$\begin{aligned} \hat{P}_0(x, y, z) = & \bar{u}_{i,j,k}^n - \frac{1}{12} \left(\bar{u}_{i+1,j+1,k+1}^n + \bar{u}_{i-1,j-1,k-1}^n - 8\bar{u}_{i,j,k}^n + \bar{u}_{i+1,j-1,k-1}^n + \bar{u}_{i+1,j-1,k+1}^n + \right. \\ & \left. \bar{u}_{i+1,j+1,k-1}^n + \bar{u}_{i-1,j+1,k+1}^n + \bar{u}_{i-1,j+1,k-1}^n + \bar{u}_{i-1,j-1,k+1}^n \right) + \\ & \frac{\bar{u}_{i+1,j+1,k+1}^n - \bar{u}_{i-1,j-1,k-1}^n}{2\Delta} \left(\frac{\Delta}{2\Delta x}(x - x_i) + \frac{\Delta}{2\Delta y}(y - y_j) + \frac{\Delta}{2\Delta z}(z - z_k) \right) + \\ & \frac{\bar{u}_{i+1,j+1,k+1}^n - \bar{u}_{i,j,k}^n + \bar{u}_{i-1,j-1,k-1}^n}{\Delta^2} \left(\frac{\Delta}{2\Delta x}(x - x_i) + \frac{\Delta}{2\Delta y}(y - y_j) + \frac{\Delta}{2\Delta z}(z - z_k) \right)^2. \end{aligned} \quad (36)$$

for the *RTF - LBBa* axis,

$$\hat{P}_{-1}(x, y, z) = \bar{u}_{i,j,k}^n + \frac{\bar{u}_{i,j,k}^n - \bar{u}_{i-1,j-1,k+1}^n}{\Delta} \left(\frac{\Delta}{2\Delta x}(x - x_i) + \frac{\Delta}{2\Delta y}(y - y_j) + \frac{\Delta}{2\Delta z}(z - z_k) \right), \quad (37)$$

$$\hat{P}_1(x, y, z) = \bar{u}_{i,j,k}^n + \frac{\bar{u}_{i+1,j+1,k-1}^n - \bar{u}_{i,j,k}^n}{\Delta} \left(\frac{\Delta}{2\Delta x}(x - x_i) + \frac{\Delta}{2\Delta y}(y - y_j) + \frac{\Delta}{2\Delta z}(z - z_k) \right), \quad (38)$$

and

$$\begin{aligned} \hat{P}_0(x, y, z) = & \bar{u}_{i,j,k}^n - \frac{1}{12} \left(\bar{u}_{i+1,j+1,k+1}^n + \bar{u}_{i-1,j-1,k-1}^n - 8\bar{u}_{i,j,k}^n + \bar{u}_{i+1,j-1,k-1}^n + \bar{u}_{i+1,j-1,k+1}^n + \right. \\ & \left. \bar{u}_{i+1,j+1,k-1}^n + \bar{u}_{i-1,j+1,k+1}^n + \bar{u}_{i-1,j+1,k-1}^n + \bar{u}_{i-1,j-1,k+1}^n \right) + \\ & \frac{\bar{u}_{i+1,j+1,k-1}^n - \bar{u}_{i-1,j-1,k+1}^n}{2\Delta} \left(\frac{\Delta}{2\Delta x}(x - x_i) + \frac{\Delta}{2\Delta y}(y - y_j) + \frac{\Delta}{2\Delta z}(z - z_k) \right) + \\ & \frac{\bar{u}_{i+1,j+1,k-1}^n - \bar{u}_{i,j,k}^n + \bar{u}_{i-1,j-1,k+1}^n}{\Delta^2} \left(\frac{\Delta}{2\Delta x}(x - x_i) + \frac{\Delta}{2\Delta y}(y - y_j) + \frac{\Delta}{2\Delta z}(z - z_k) \right)^2. \end{aligned} \quad (39)$$

for the *RTBa* – *LBF* axis,

$$\hat{P}_{-1}(x, y, z) = \bar{u}_{i,j,k}^n + \frac{\bar{u}_{i,j,k}^n - \bar{u}_{i-1,j+1,k-1}^n}{\Delta} \left(\frac{\Delta}{2\Delta x}(x - x_i) + \frac{\Delta}{2\Delta y}(y - y_j) + \frac{\Delta}{2\Delta z}(z - z_k) \right), \quad (40)$$

$$\hat{P}_1(x, y, z) = \bar{u}_{i,j,k}^n + \frac{\bar{u}_{i+1,j-1,k+1}^n - \bar{u}_{i,j,k}^n}{\Delta} \left(\frac{\Delta}{2\Delta x}(x - x_i) + \frac{\Delta}{2\Delta y}(y - y_j) + \frac{\Delta}{2\Delta z}(z - z_k) \right), \quad (41)$$

and

$$\begin{aligned} \hat{P}_0(x, y, z) = & \bar{u}_{i,j,k}^n - \frac{1}{12} \left(\bar{u}_{i+1,j+1,k+1}^n + \bar{u}_{i-1,j-1,k-1}^n - 8\bar{u}_{i,j,k}^n + \bar{u}_{i+1,j-1,k-1}^n + \bar{u}_{i+1,j-1,k+1}^n + \right. \\ & \left. \bar{u}_{i+1,j+1,k-1}^n + \bar{u}_{i-1,j+1,k+1}^n + \bar{u}_{i-1,j+1,k-1}^n + \bar{u}_{i-1,j-1,k+1}^n \right) + \\ & \frac{\bar{u}_{i+1,j-1,k+1}^n - \bar{u}_{i-1,j+1,k-1}^n}{2\Delta} \left(\frac{\Delta}{2\Delta x}(x - x_i) + \frac{\Delta}{2\Delta y}(y - y_j) + \frac{\Delta}{2\Delta z}(z - z_k) \right) + \\ & \frac{\bar{u}_{i+1,j-1,k+1}^n - \bar{u}_{i,j,k}^n + \bar{u}_{i-1,j+1,k-1}^n}{\Delta^2} \left(\frac{\Delta}{2\Delta x}(x - x_i) + \frac{\Delta}{2\Delta y}(y - y_j) + \frac{\Delta}{2\Delta z}(z - z_k) \right)^2. \end{aligned} \quad (42)$$

for the *RBF* – *LTBa* axis, and

$$\hat{P}_{-1}(x, y, z) = \bar{u}_{i,j,k}^n + \frac{\bar{u}_{i,j,k}^n - \bar{u}_{i-1,j+1,k+1}^n}{\Delta} \left(\frac{\Delta}{2\Delta x}(x - x_i) + \frac{\Delta}{2\Delta y}(y - y_j) + \frac{\Delta}{2\Delta z}(z - z_k) \right), \quad (43)$$

$$\hat{P}_1(x, y, z) = \bar{u}_{i,j,k}^n + \frac{\bar{u}_{i+1,j-1,k-1}^n - \bar{u}_{i,j,k}^n}{\Delta} \left(\frac{\Delta}{2\Delta x}(x - x_i) + \frac{\Delta}{2\Delta y}(y - y_j) + \frac{\Delta}{2\Delta z}(z - z_k) \right), \quad (44)$$

and

$$\begin{aligned}
\hat{P}_0(x, y, z) = & \bar{u}_{i,j,k}^n - \frac{1}{12} \left(\bar{u}_{i+1,j+1,k+1}^n + \bar{u}_{i-1,j-1,k-1}^n - 8\bar{u}_{i,j,k}^n + \bar{u}_{i+1,j-1,k-1}^n + \bar{u}_{i+1,j-1,k+1}^n + \right. \\
& \left. \bar{u}_{i+1,j+1,k-1}^n + \bar{u}_{i-1,j+1,k+1}^n + \bar{u}_{i-1,j+1,k-1}^n + \bar{u}_{i-1,j-1,k+1}^n \right) + \\
& \frac{\bar{u}_{i+1,j-1,k-1}^n - \bar{u}_{i-1,j+1,k+1}^n}{2\Delta} \left(\frac{\Delta}{2\Delta x} (x - x_i) + \frac{\Delta}{2\Delta y} (y - y_j) + \frac{\Delta}{2\Delta z} (z - z_k) \right) + \\
& \frac{\bar{u}_{i+1,j-1,k-1}^n - \bar{u}_{i,j,k}^n + \bar{u}_{i-1,j+1,k+1}^n}{\Delta^2} \left(\frac{\Delta}{2\Delta x} (x - x_i) + \frac{\Delta}{2\Delta y} (y - y_j) + \frac{\Delta}{2\Delta z} (z - z_k) \right)^2.
\end{aligned} \tag{45}$$

for the *RBBa - LTF* axis.

The weights in Eqn. (33) are calculated in the exact same manner as in Eqn. (25). With regard to indicators and corner values, for example, for the *RTF - LBBa* axis they read as

$$\begin{aligned}
IS_{-1} &= (\bar{u}_{i,j,k}^n - \bar{u}_{i-1,j-1,k-1}^n)^2 \\
IS_1 &= (\bar{u}_{i+1,j+1,k+1}^n - \bar{u}_{i,j,k}^n)^2 \\
IS_0 &= \frac{13}{3} (\bar{u}_{i+1,j+1,k+1}^n - 2\bar{u}_{i,j,k}^n + \bar{u}_{i-1,j-1,k-1}^n)^2 + \frac{1}{4} (\bar{u}_{i+1,j+1,k+1}^n - \bar{u}_{i-1,j-1,k-1}^n)^2
\end{aligned} \tag{46}$$

and

$$\begin{aligned}
u_{i,j,k}^{RTF} = & w_{-1} \left[\bar{u}_{i,j,k}^n + \frac{1}{2} (\bar{u}_{i,j,k}^n - \bar{u}_{i-1,j-1,k-1}^n) \right] + w_0 \left[\bar{u}_{i,j,k}^n \right. \\
& - \frac{1}{12} (\bar{u}_{i+1,j+1,k+1}^n + \bar{u}_{i-1,j-1,k-1}^n - 8\bar{u}_{i,j,k}^n + \bar{u}_{i+1,j-1,k-1}^n + \bar{u}_{i+1,j-1,k+1}^n + \bar{u}_{i+1,j+1,k-1}^n \\
& \left. + \bar{u}_{i-1,j+1,k+1}^n + \bar{u}_{i-1,j+1,k-1}^n + \bar{u}_{i-1,j-1,k+1}^n) \right. \\
& \left. + \frac{1}{2} (\bar{u}_{i+1,j+1,k+1}^n - \bar{u}_{i-1,j-1,k-1}^n) + \frac{1}{4} (\bar{u}_{i+1,j+1,k+1}^n - \bar{u}_{i,j,k}^n + \bar{u}_{i-1,j-1,k-1}^n) \right] \\
& + w_1 \left[\bar{u}_{i,j,k}^n + \frac{1}{2} (\bar{u}_{i+1,j+1,k+1}^n - \bar{u}_{i,j,k}^n) \right] \tag{47}
\end{aligned}$$

and

$$\begin{aligned}
u_{i,j,k}^{LBBa} &= w_{-1} \left[\bar{u}_{i,j,k}^n - \frac{1}{2} \left(\bar{u}_{i,j,k}^n - \bar{u}_{i-1,j-1,k-1}^n \right) \right] + w_0 \left[\bar{u}_{i,j,k}^n \right. \\
&- \frac{1}{12} \left(\bar{u}_{i+1,j+1,k+1}^n + \bar{u}_{i-1,j-1,k-1}^n - 8\bar{u}_{i,j,k}^n + \bar{u}_{i+1,j-1,k-1}^n + \bar{u}_{i+1,j-1,k+1}^n + \bar{u}_{i+1,j+1,k-1}^n \right. \\
&\quad \left. \left. + \bar{u}_{i-1,j+1,k+1}^n + \bar{u}_{i-1,j+1,k-1}^n + \bar{u}_{i-1,j-1,k+1}^n \right) \right. \\
&- \frac{1}{2} \left(\bar{u}_{i+1,j+1,k+1}^n - \bar{u}_{i-1,j-1,k-1}^n \right) + \frac{1}{4} \left(\bar{u}_{i+1,j+1,k+1}^n - \bar{u}_{i,j,k}^n + \bar{u}_{i-1,j-1,k-1}^n \right) \left. \right] \\
&\quad + w_1 \left[\bar{u}_{i,j,k}^n - \frac{1}{2} \left(\bar{u}_{i+1,j+1,k+1}^n - \bar{u}_{i,j,k}^n \right) \right] \quad (48)
\end{aligned}$$

and for the $RTBa - LBF$ axis they read as

$$\begin{aligned}
IS_{-1} &= (\bar{u}_{i,j,k}^n - \bar{u}_{i-1,j-1,k+1}^n)^2 \\
IS_1 &= (\bar{u}_{i+1,j+1,k-1}^n - \bar{u}_{i,j,k}^n)^2 \\
IS_0 &= \frac{13}{3} (\bar{u}_{i+1,j+1,k-1}^n - 2\bar{u}_{i,j,k}^n + \bar{u}_{i-1,j-1,k+1}^n)^2 + \frac{1}{4} (\bar{u}_{i+1,j+1,k-1}^n - \bar{u}_{i-1,j-1,k+1}^n)^2 \\
&\hspace{15em} (49)
\end{aligned}$$

and

$$\begin{aligned}
u_{i,j,k}^{RTBa} &= w_{-1} \left[\bar{u}_{i,j,k}^n + \frac{1}{2} \left(\bar{u}_{i,j,k}^n - \bar{u}_{i-1,j-1,k+1}^n \right) \right] + w_0 \left[\bar{u}_{i,j,k}^n \right. \\
&- \frac{1}{12} \left(\bar{u}_{i+1,j+1,k+1}^n + \bar{u}_{i-1,j-1,k-1}^n - 8\bar{u}_{i,j,k}^n + \bar{u}_{i+1,j-1,k-1}^n + \bar{u}_{i+1,j-1,k+1}^n + \bar{u}_{i+1,j+1,k-1}^n \right. \\
&\quad \left. \left. + \bar{u}_{i-1,j+1,k+1}^n + \bar{u}_{i-1,j+1,k-1}^n + \bar{u}_{i-1,j-1,k+1}^n \right) \right. \\
&+ \frac{1}{2} \left(\bar{u}_{i+1,j+1,k-1}^n - \bar{u}_{i-1,j-1,k+1}^n \right) + \frac{1}{4} \left(\bar{u}_{i+1,j+1,k-1}^n - \bar{u}_{i,j,k}^n + \bar{u}_{i-1,j-1,k+1}^n \right) \left. \right] \\
&\quad + w_1 \left[\bar{u}_{i,j,k}^n + \frac{1}{2} \left(\bar{u}_{i+1,j+1,k-1}^n - \bar{u}_{i,j,k}^n \right) \right] \quad (50)
\end{aligned}$$

and

$$\begin{aligned}
u_{i,j,k}^{LBF} = & w_{-1} \left[\bar{u}_{i,j,k}^n - \frac{1}{2} \left(\bar{u}_{i,j,k}^n - \bar{u}_{i-1,j-1,k+1}^n \right) \right] + w_0 \left[\bar{u}_{i,j,k}^n \right. \\
& - \frac{1}{12} \left(\bar{u}_{i+1,j+1,k+1}^n + \bar{u}_{i-1,j-1,k-1}^n - 8\bar{u}_{i,j,k}^n + \bar{u}_{i+1,j-1,k-1}^n + \bar{u}_{i+1,j-1,k+1}^n + \bar{u}_{i+1,j+1,k-1}^n \right. \\
& \quad \left. \left. + \bar{u}_{i-1,j+1,k+1}^n + \bar{u}_{i-1,j+1,k-1}^n + \bar{u}_{i-1,j-1,k+1}^n \right) \right. \\
& \left. - \frac{1}{2} \left(\bar{u}_{i+1,j+1,k-1}^n - \bar{u}_{i-1,j-1,k+1}^n \right) + \frac{1}{4} \left(\bar{u}_{i+1,j+1,k-1}^n - \bar{u}_{i,j,k}^n + \bar{u}_{i-1,j-1,k+1}^n \right) \right] \\
& + w_1 \left[\bar{u}_{i,j,k}^n - \frac{1}{2} \left(\bar{u}_{i+1,j+1,k-1}^n - \bar{u}_{i,j,k}^n \right) \right] \quad (51)
\end{aligned}$$

The details regarding the indicator functions and the corner values corresponding to the rest of the diagonal axes (*RBF-LTBa* and *RBBa-LTF*) are not provided here in order to avoid repetition, but can be deduced in a straightforward manner. The next section presents specific test cases related to the governing equations presented above along with a parallel scaling analysis of the implementation of such schemes on multiple platforms.

5 Numerical Test Cases

This section presents results from the solutions of Eqn. (2) and systems of equations Eqns. (3)-(5) and Eqns. (6)-(9) in applications of a scalar convection problem, the Richtmeyer-Meshkov instability, and the Orszag-Tang vortex problem, respectively. For all the calculations presented here, we choose a uniform grid in physical space. For temporal discretization, the third-order Strong Stability-preserving (SSP) Runge-Kutta [23,24] is used and the time step is dynamically calculated to satisfy the CFL restriction given by

$$\Delta t = \frac{\text{CFL}}{\sqrt{\frac{(\max |a_{i,j,k}|)^2}{(\Delta x)^2} + \frac{(\max |b_{i,j,k}|)^2}{(\Delta y)^2} + \frac{(\max |c_{i,j,k}|)^2}{(\Delta z)^2}}} \quad (52)$$

where $a_{i,j,k}$, $b_{i,j,k}$ and $c_{i,j,k}$ are the speeds of propagation (Eqns. (12)). The CFL number was chosen to be 0.5 in all the cases presented here.

5.1 *Single scalar equation: Inviscid Burgers equation*

The presentation of three-dimensional semi-discrete schemes, formulated in the previous section begins with the solution of a single scalar equation given by Eqn. (2). The equation is solved in a $3D$ computational domain of size $1 \times 1 \times 1$ with a total of up to 100^3 points, and the initial conditions are such that the variable u is given by

$$u = 0.5; \quad 0.1 \leq x \leq 0.5, \quad 0.1 \leq y \leq 0.5, \quad 0.1 \leq z \leq 0.5, \quad (53)$$

and zero elsewhere.

Firstly Fig. 4 presents instantaneous solutions at time $t = 0.4$ for two different grid sizes 50^3 and 100^3 . Very slight differences between the solutions exist indicating a grid-independent solution. The rest of the results presented in this section are those with the fine grid (100^3). Figures 5 and 6 present solutions of Eqn. (2) using the polynomial reconstructions *without* and *with* diagonal smoothing respectively. Iso-surfaces at two different values and the slices in two different directions are shown at various times. The non-zero region or "cube" moves towards the corner $(1, 1, 1)$ as time progresses. There is a significant difference between the evolution of the solutions in the two cases. The edges of the "cube" are considerably smoothed in the case where a polynomial reconstruction is applied in the diagonal directions (Fig. 6). This leads to an increased dissipation of the sharp discontinuities (or in this case the edges of

the "cube") and hence the smoothing.

5.2 Parallel performance analysis for system of equations

The computational requirements for the solution of hyperbolic problems could become prohibitive in the case of three-dimensional, geometrically complex enclosures. These requirements increase further when realistic fluid flows like viscous or turbulent flows are considered, thereby requiring larger computational effort and memory. Recent developments in high-performance computing promise a substantial increase in computational speed and offer new possibilities for more accurate simulations. Three-dimensional domain decomposition is used to speed the calculations, where the computational domain is decomposed into a number of rectangular blocks with each processor being responsible for a single block. An example of this decomposition can be seen by the gaps in the grid in Fig. 7 for the specific case of 16 processors.

Most of the calculations in the interior of each of the sub-domains are independent of the domain decomposition, and can continue as if being performed serially. Problems arise near the sub-domain boundaries where, for example, finite differences calculated adjacent to the subdomain boundaries may need several points outside the subdomain. To support these circumstances, two rows of "ghost points" are carried along with the interior solutions that contain copies of the interior solution from the neighboring sub-domain. These points are exchanged and updated from neighboring processors as needed to ensure that all near-wall calculations are performed with current variable values.

If a uniform grid is used, then the sub domains in each direction will contain equal number of grid points. However, for a non-uniform grid, the the division locations between the sub-domains need to be selected to provide good load balancing, or an equivalent amount of work for each processor in each time step. Hence, for the purpose of a scaling analysis, Fig. 8 illustrates the CPU time, parallel speedup, $S_p = T_{serial}/T_{parallel}$, and the parallel efficiency, $E_p = S_p/p$, where T_{serial} , $T_{parallel}$ and p are the CPU time for serial and parallel runs and the number of processors respectively. The scaling analysis is presented for the numerical solutions of the Euler hydrodynamic system presented above (Eqns. (3)- (5)). Diagnostics for two different problem sizes are presented, one with 128^3 , while the other with 256^3 number of points. The simulations were conducted on the IBM Blue Gene architecture at Argonne National Labs. Due to the high memory requirements of the code, the lowest number of processors on which a 128^3 simulation can be run is 16, while the corresponding number for the 256^3 simulation is 32. In order to present a complete scaling analysis, i.e. to calculate speedup and efficiency, it is assumed that these quantities are ideal up to 16 and 32 processors for the 128 and 256^3 simulations, respectively.

Figure 8 shows the simulation time for 10 time steps on a log scale, where the point corresponding to a single processor was in fact extrapolated from the nearest point assuming ideal efficiency (100%). The CPU time decreases linearly with number of processors which is encouraging. On the same figure speedup and efficiency are close to ideal (red dashed line), with efficiency values ranging between 94% and 100%.

5.3 Euler system of equations: Richtmeyer-Meshkov instability

The first 3D realistic problem that is considered here is the evolution of the Richtmeyer-Meshkov instability (RMI) [25,26]. RMI arises when a shock passes through an interface between two fluids of widely ranging densities. A generic feature of these systems, as is the case for fluid turbulence in general, is the existence of fluctuations on multiple length scales. Three-dimensional simulations of the re-shocked RMI modeled after the Mach 1.21 experiment of Collins and Jacobs [27] are presented in the present work. The simulations use the 3rd order CWENO reconstruction method without diagonal smoothing (to avoid excess dissipation resulting from it) using $1024 \times 512 \times 512$ grid points on a domain of $17.8 \times 8.9 \times 8.9$ cm³. For test purposes, and in order to have a higher resolution, the domain size here in these simulations is more than 50% smaller in the X -direction as compared to experiments.

The initial conditions were adapted from the Mach 1.21 air/ SF_6 experimental shock tube configuration of Collins and Jacobs [27]. The adiabatic exponent $\gamma = 1.24815$ corresponding to an air mixture was used. The ratio of densities is given by $\frac{\rho_{SF_6}}{\rho_{air}} = 4.063$. The initial sinusoidal interface $\eta(y, z) = a_o \sin(2\pi y/\lambda) \sin(2\pi z/\lambda)$ had pre-shock amplitude $a_o = 0.2$ cm and wavelength $\lambda = 5.933$ cm. An initial diffusion layer thickness of $\delta = 0.5$ cm was used, where the thickness function is $S(x, y, z) = 1$ if $d \leq 0$, $= \exp(-\alpha |d|^\beta)$ if $0 < d < 1$ and 0 otherwise. $d = (x_s + \eta(y, z) + \delta - x)/(2\delta)$, and $\alpha = -\ln\beta$ (β is machine zero).

The following boundary conditions were used: (a) inflow at the test section entrance in the streamwise X -direction; (b) reflecting at the end wall of the

test section in the streamwise direction, and; (c) periodic in the Y and Z -directions corresponding to the cross-section of the test section. The reflecting boundary condition is implemented by reversing the normal component of the velocity vector: $u(x, t) = -u(x, t)$ at $x = 17.8$ cm (maximum in the streamwise direction) and at the ghost points, which is exact and does not generate spurious noise [28].

Figures 9, 10, and 11 show the instantaneous contour slices of density, velocity, and isosurfaces of density, respectively, at times given by $t = 1$ ms, $t = 2$ ms, $t = 3$ ms and $t = 4$ ms. As the RMI instability develops, spikes of SF_6 fall into the air. Following this initial growth, the spikes roll-up and additional complex structures begin to appear. The results presented here are qualitatively similar to other studies, e.g. [28].

5.4 *Ideal Magnetohydrodynamic (MHD) equations: Orszag-Tang vortex system*

Our next 3D problem, that is investigated is a 3D MHD problem, the Orszag-Tang-type problem [29]. The evolution of the vortex system involves the interaction between several shock waves traveling at various speed regimes [30,31], which makes the problem especially attractive for numerical experiments. The initial data for this problem are the following:

$$\begin{aligned}
 \rho &= \gamma^2 \\
 p &= \gamma \\
 \mathbf{u} &= (-\sin y \sin z, \quad \sin x \sin z, \quad 0) \\
 \mathbf{B} &= (-\sin y \sin z, \quad \sin 2x \sin z, \quad \sin 2x \sin y)
 \end{aligned}
 \tag{54}$$

with $0 \leq x, y, z \leq 2\pi$, where $\gamma = 5/3$. Again, grid independence is demonstrated in Fig. 12 through density contours on slices across the centerlines planes on coarse (128^3) and fine grids (256^3). The results presented here in this section are those computed on the 256^3 grid using the CWENO reconstruction without diagonal smoothing.

A way of demonstrating the accuracy of a numerical method is to determine whether the solenoidal constraint $\nabla \cdot \mathbf{B} = 0$ is maintained throughout the simulation. Since $\nabla \cdot \mathbf{B} = 0$ initially, theoretically it should remain so throughout the simulation. However, the accumulation of numerical errors can usually lead to non-physical phenomena known as magnetic monopoles (when $\nabla \cdot \mathbf{B}$ is not equal to 0). The schemes presented here when first introduced in [6] in a 1D and 2D framework did not require an explicit enforcement of the solenoidal constraint for producing stable and reasonably accurate solutions, and hence no such treatment is used here either. Figure 13 shows the surface plots of $\nabla \cdot \mathbf{B}$ on all the Z -surfaces at a certain instant in time. The maximum value of the magnitude of $\nabla \cdot \mathbf{B}$ at this instant is 0.41, which is actually representative of the entire simulation. Figure 14 shows a density isosurface. Fig. 15 shows contours of density on three slices across the $x = y = z = \pi$ planes and Fig. 16 shows the 2D magnetic field vector colored by magnetic field magnitude. These results demonstrate the ability of such higher-order central schemes to resolve the shocks that the vortex system develops while maintaining the simplicity and ease of implementation typical of this black-box type of finite difference schemes.

6 Conclusions

Extensions of the semi-discrete schemes of Balbas and Tadmor [6] to $3D$ are presented and tested for the first time in this paper. The numerical test cases chosen include evolution of (a) a single scalar equation or an inviscid Burgers equation, (b) the Richtmeyer-Meshkov instability (RMI) using Euler hydrodynamic equations, and (c) the Orszag-Tang vortex system using ideal magnetohydrodynamic equations. Grid independence was demonstrated for two of the three cases presented here. The single scalar equation test case results indicated excessive dissipation when diagonal smoothing was applied. Parallel scaling analysis showed almost ideal efficiencies and speedups based on the assumption that they hold ideal values up until 16 processors. The results obtained with these schemes for the Richtmeyer-Meshkov instability and the Orszag-Tang vortex system confirm the ability of this type of solver to approximate the discontinuous solutions of Eulerian gas dynamics and ideal magnetohydrodynamics equations.

7 Acknowledgements

We would like to thank Jorge Balbas for an insightful discussion on these numerical methods early on. We would also like to thank Argonne National Labs and the National Center for Super Computing Applications (NCSA) for providing computing resources for testing the schemes and obtaining the results presented in this paper.

References

- [1] R. J. LeVeque, Numerical Methods for Conservation Laws, Lectures in Mathematics, Birkhauser Verlag, Basel, 1992.
- [2] H. Nessyahu, E. Tadmor, Non-oscillatory central differencing for hyperbolic conservation laws, *J. Comp. Phys.* 87 (1990) 408–463.
- [3] D. Levy, G. Puppo, G. Russo, Compact central weno schemes for multidimensional conservation laws, *SIAM J. Sci. Comp.* 22 (2000) 656–672.
- [4] A. Kurganov, D. Levy, A third-order semi-discrete central scheme for conservation laws and convection-diffusion equation, *SIAM J. Sci. Comp.* 22 (2000) 1461–1488.
- [5] Y. Liu, Central schemes on overlapping cells, *J. Comp. Phys.* 209 (2005) 82–104.
- [6] J. Balbas, E. Tadmor, Non-oscillatory central schemes for one- and two-dimensional mhd equations. II: High-order semi-discrete schemes, *SIAM J. Sci. Comp.* 28 (2006) 533–560.
- [7] K. O. Friedrichs, P. D. Lax, Systems of conservation equations with a convex extension, *Proc. Nat. Acad. Sci* 68 (1971) 1686–1688.
- [8] X. D. Liu, E. Tadmor, Third-order non-oscillatory central scheme for hyperbolic conservation laws, *Numer. Math.* 79 (1998) 397–425.
- [9] D. Levy, G. Puppo, G. Russo, Central weno schemes for hyperbolic systems of conservation laws, *Math. Model. Num. Analysis.* 33 (1999) 547–571.
- [10] D. Levy, G. Puppo, G. Russo, A fourth-order central weno scheme for multi-dimensional hyperbolic systems of conservation laws, *SIAM J. Sci. Comp.* 24 (2002) 480–506.

- [11] G. S. Jiang, E. Tadmor, Nonoscillatory central schemes for multidimensional hyperbolic conservation laws, *SIAM J. Sci. Comp.* 19 (1998) 1892–1917.
- [12] D. Levy, G. Puppo, G. Russo, A third order central weno scheme for 2d conservation laws, *App. Num. Math.* 33 (2000) 415–421.
- [13] B. VanLeer, Towards the ultimate conservative difference scheme , V. A second order sequel to godunov’s method, *J. Comp. Phys.* 32 (1979) 101–136.
- [14] A. Kurganov, P. Rosenau, Effects of saturating dissipation in burgers-type equations, *Comm. Pure Appl. Math.* 50 (1997) 753–771.
- [15] A. Kurganov, D. Levy, P. Rosenau, On burgers-type equations with nonmonotonic dissipative fluxes, *Comm. Pure Appl. Math.* 51 (1998) 443–473.
- [16] A. Kurganov, E. Tadmor, New high-resolution central schemes for nonlinear conservation laws and convection-diffusion equations, *Comm. Pure Appl. Math.* 50 (1997) 753–771.
- [17] G. S. Jiang, D. Levy, C. T. Lin, S. Osher, E. Tadmor, High-resolution non-oscillatory central schemes with non-staggered grids for hyperbolic conservation laws, *SIAM J. Num. Anal.* 35 (1998) 2147–2168.
- [18] A. Harten, B. Engquist, S. Osher, S. Chakravarthy, Uniformly high-order accurate essentially non-oscillatory schemes III, *J. Comp. Phys.* 71 (1987) 231–303.
- [19] W. Shu, Numerical experiments on the accuracy of eno and modified eno schemes, *SIAM J. Sci. Comp.* 5 (1990) 127–149.
- [20] G. S. Jiang, W. Shu, Efficient implementation of weighted eno schemes, *J. Comp. Phys.* 126 (1996) 202–228.
- [21] J. Balbas, E. Tadmor, C. Wu, Non-oscillatory central schemes for one- and two-dimensional mhd equations, *J. Comp. Phys.* 201 (2004) 261–285.

- [22] A. Kurganov, G. Petrova, A third-order semi-discrete genuinely multidimensional central scheme for hyperbolic conservation laws and related problems, *Numerische Mathematik* 88 (2001) 683–729.
- [23] C. W. Shu, Total-variation-diminishing time discretizations, *SIAM J. Sci. Comput.* 9 (1988) 1073–1084.
- [24] S. Gottlieb, C.-W. Shu, E. Tadmor, Strong stability-preserving high-order time discretization methods, *SIAM Review* 43 (1) (2001) 89–112.
- [25] R. Richtmeyer, Taylor instability in shock acceleration of compressible fluids, *Comm. Pure Appl. Math.* 13 (1960) 297–319.
- [26] E. Meshkov, Instability of the interface of two gases accelerated by a shock wave, *Sov. Fluid Dyn.* 4 (1969) 101–108.
- [27] B. D. Collins, J. W. Jacobs, Plif flow visualization and measurements of the richtmeyer-meshkov instability of an air/ SF_6 interface, *J. Fluid Mech.* 464 (2002) 113–136.
- [28] M. Latini, O. Schilling, W. S. Don, Effects of WENO flux reconstruction order and spatial resolution on reshocked two-dimensional richtmeyer-meshkov instability, *J. Comp. Phys.* 221 (2007) 805–836.
- [29] S. Orszag, C. Tang, Small-scale structure of two-dimensional magnetohydrodynamic turbulence, *J. Fluid Mech.* 90 (1979) 129–145.
- [30] R. B. Dahlburg, J. M. Picone, Evolution of the Orszag-Tang vortex system in a compressible medium I. Initial average subsonic flow, *Phys. Fluids. B* 1 (1989) 2153–2165.
- [31] G. S. Jiang, C. C. Wu, A high-order weno finite difference scheme for the equations for ideal magnetohydrodynamics, *J. Comp. Phys.* 150 (1999) 561–594.

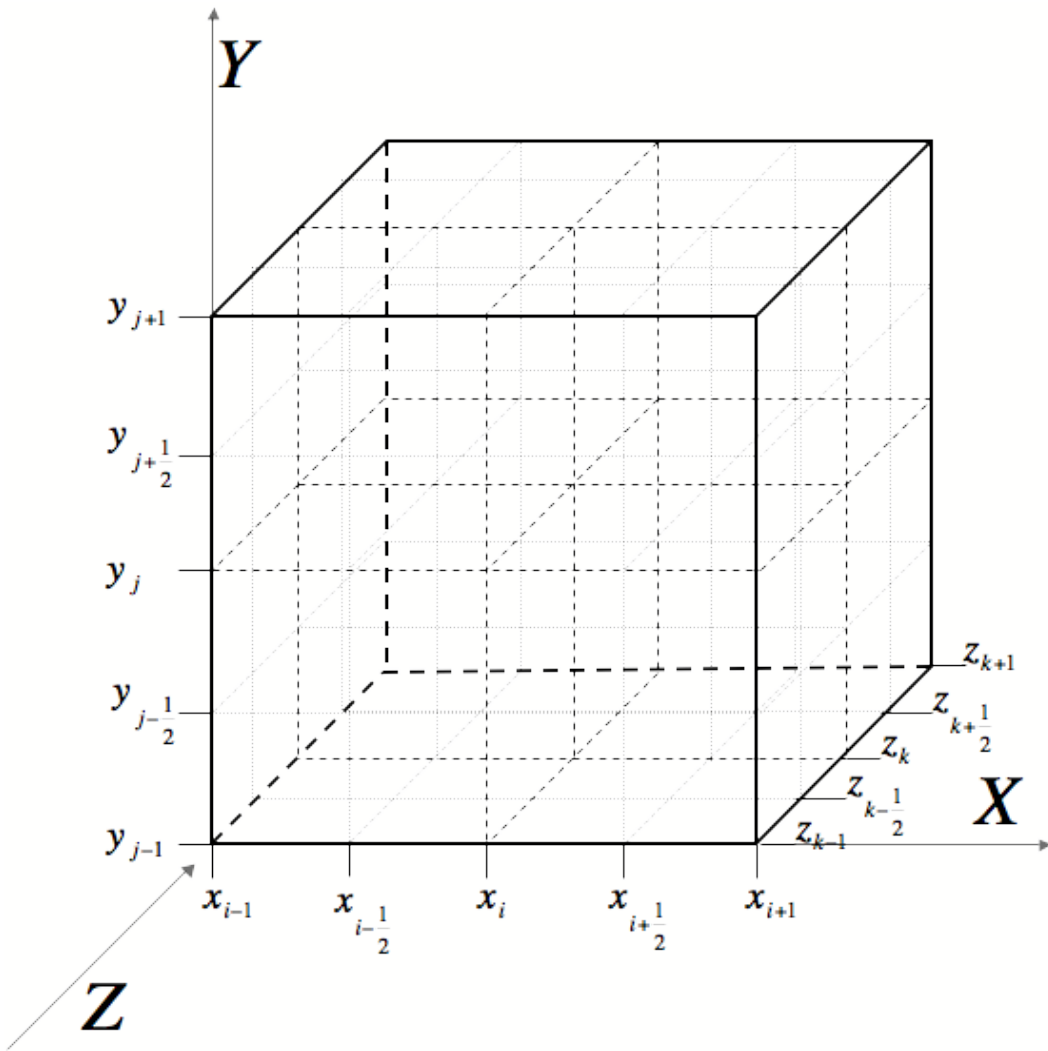


Fig. 1. Modified central differencing in three-space dimensions.

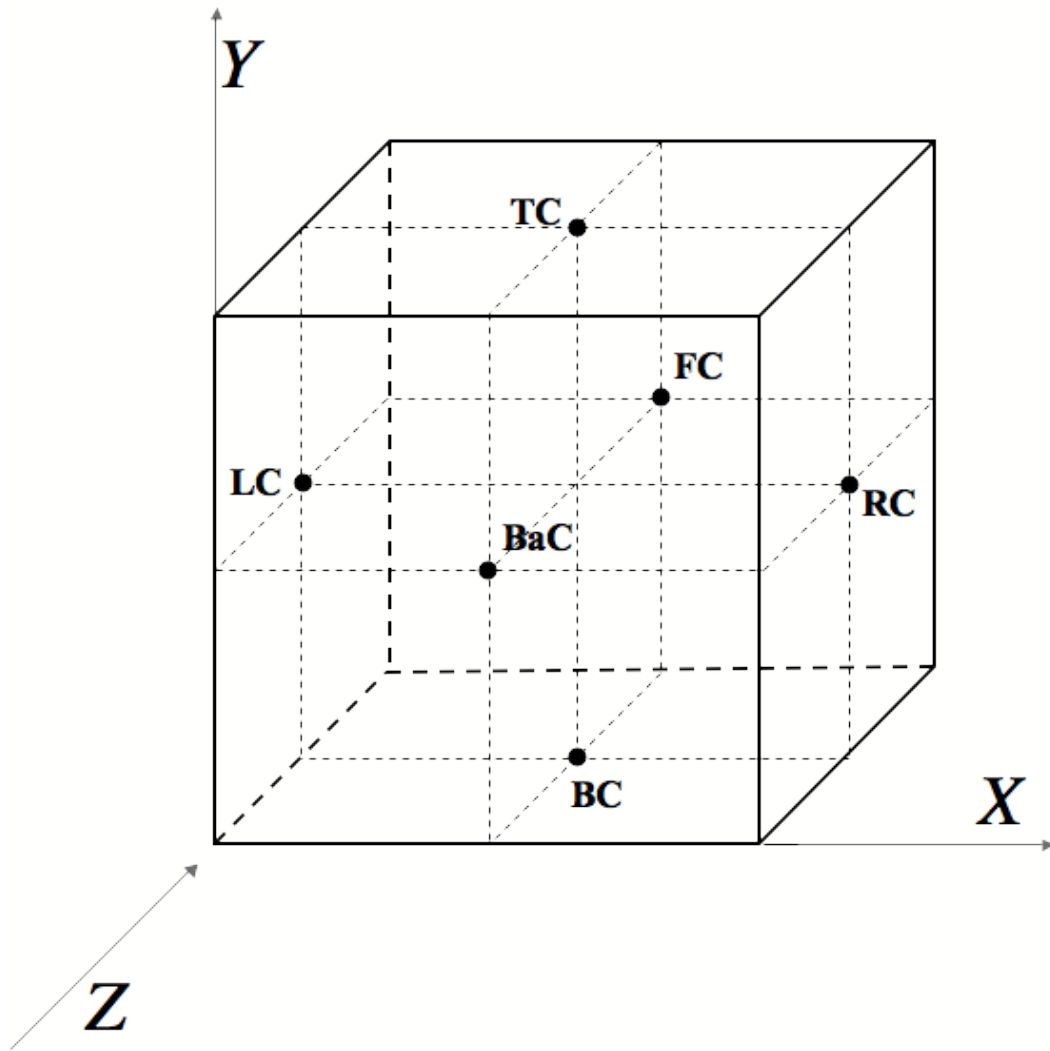


Fig. 2. Reconstructions in the x -, y - and z - directions.

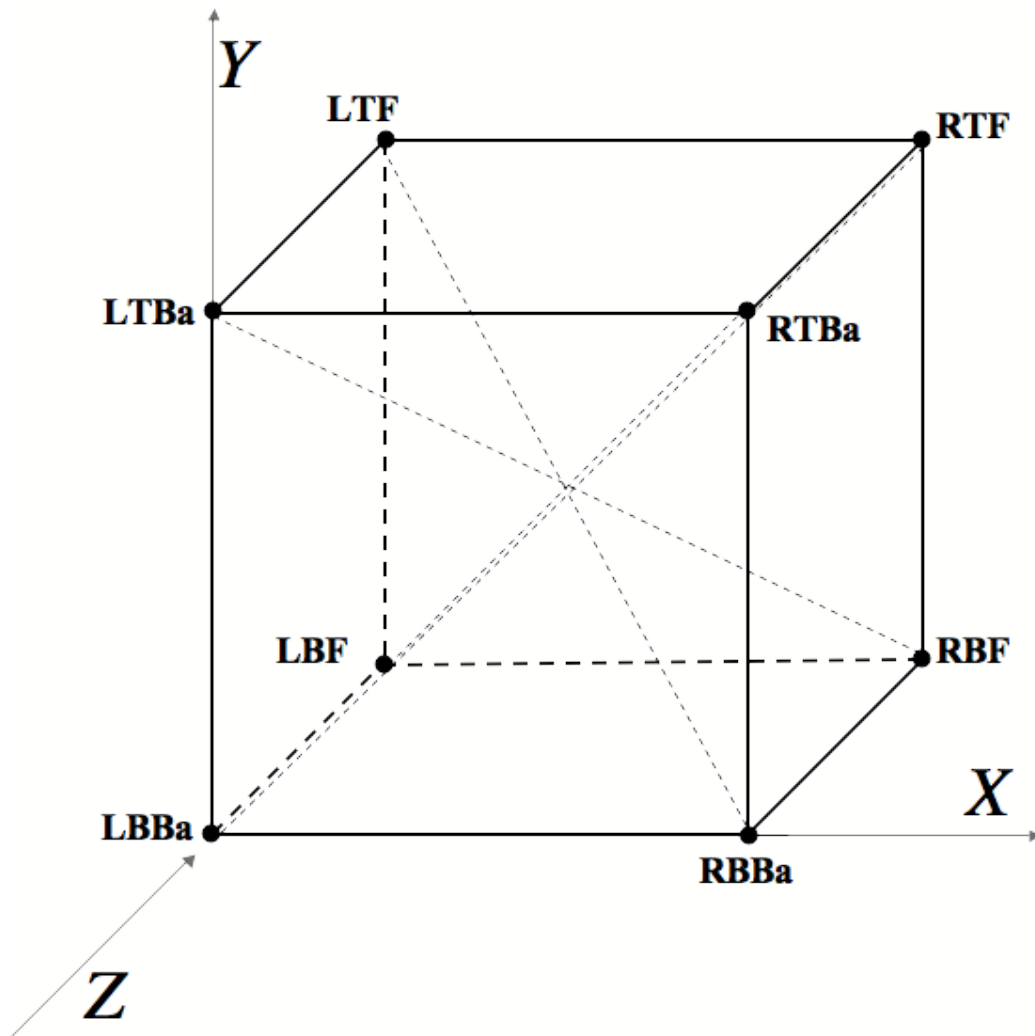


Fig. 3. Reconstructions in the diagonal directions.

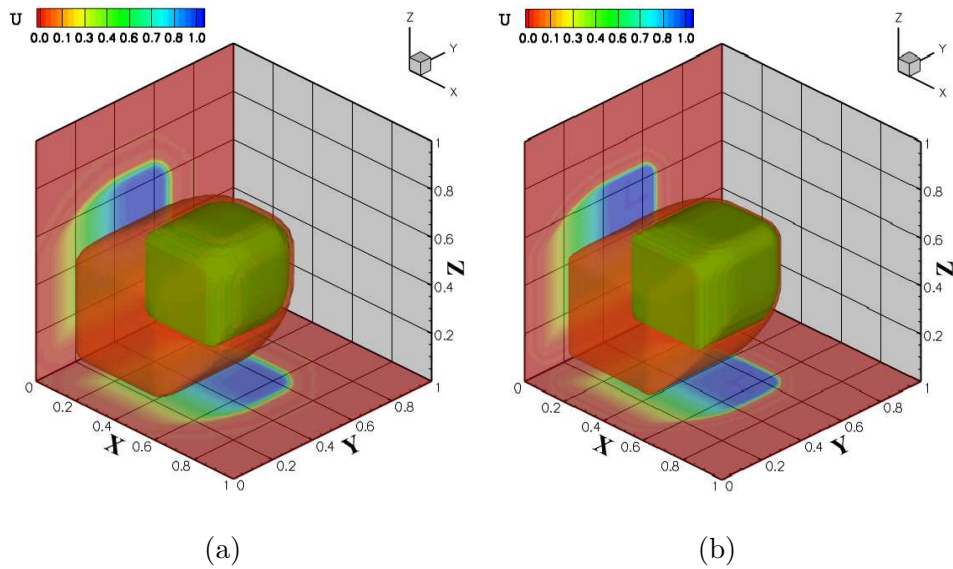


Fig. 4. Instantaneous solutions of the non-linear scalar equation Eqn. (2) using the CWENO polynomial reconstruction *WITHOUT* diagonal smoothing at time $t = 0.4$ for two different grid sizes: 50^3 (left) and 100^3 (right). Shown are iso-surfaces at two values 0.5 and 0.05, along with slices along $X = 0.3$ and $Z = 0.3$, which are projected to the end of the domain.

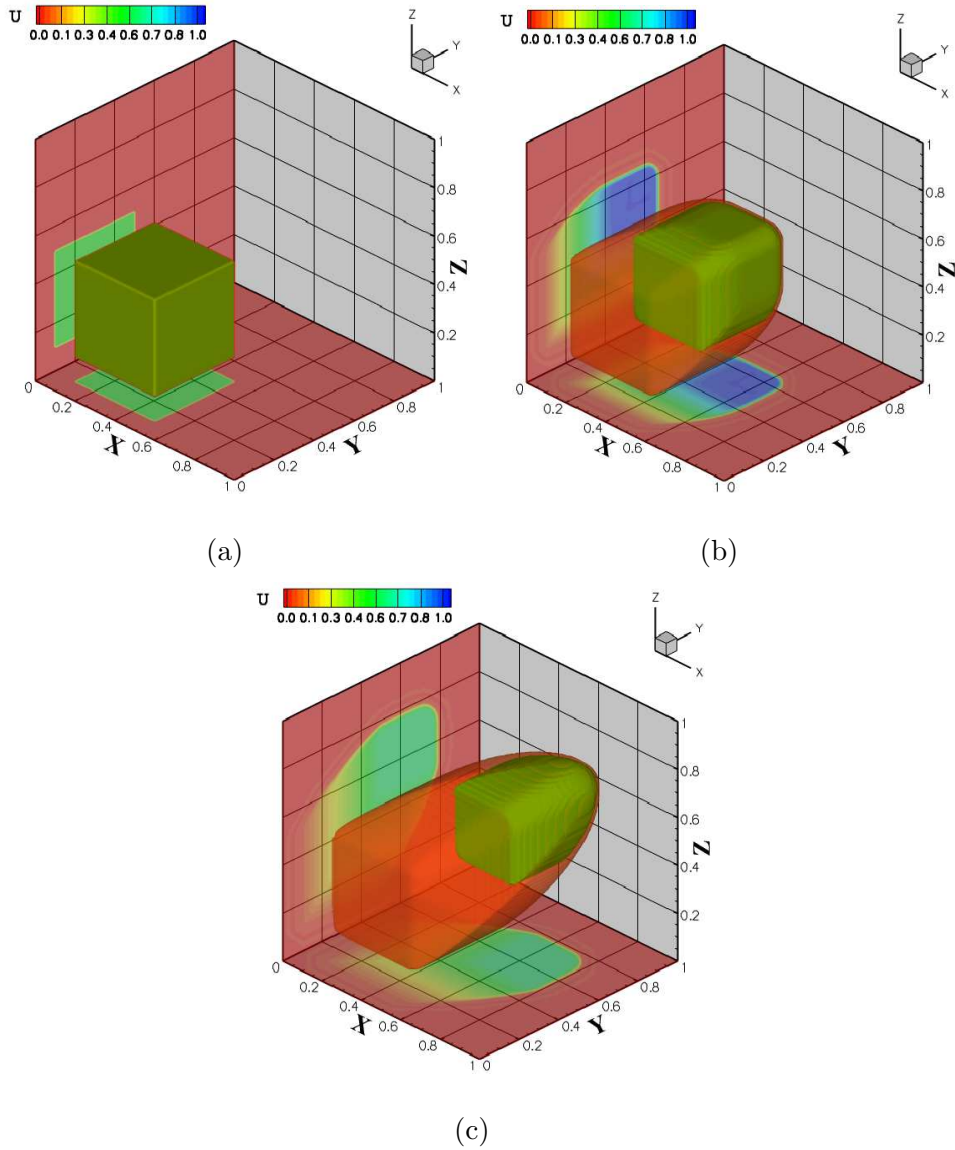


Fig. 5. Same as Fig. 4 but these solutions using the CWENO polynomial reconstruction *WITHOUT* diagonal smoothing at times (a) $t = 0$ (b) $t = 0.4$ and (c) $t = 0.8$.

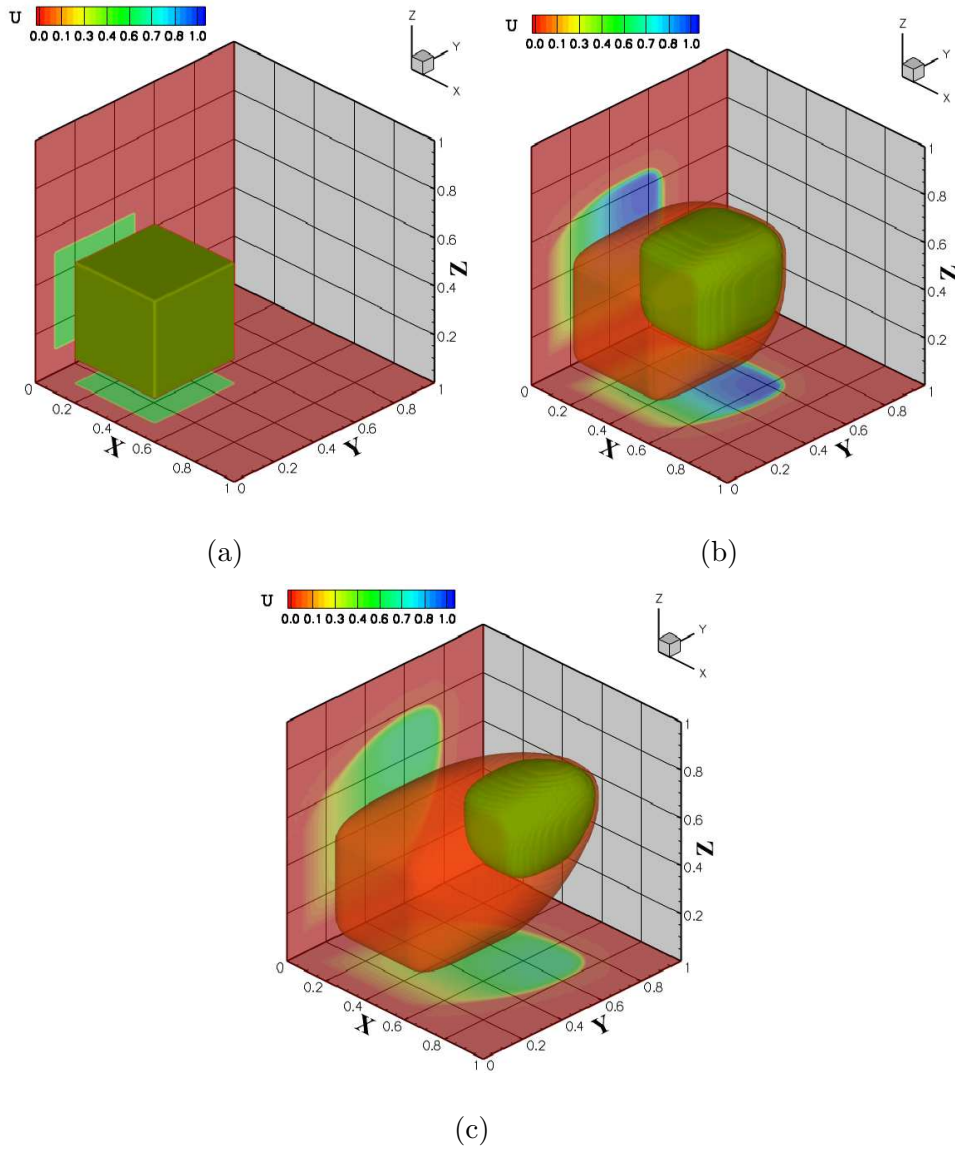


Fig. 6. Same as Fig. 5, but these are solutions using the CWENO polynomial reconstruction *WITH* diagonal smoothing

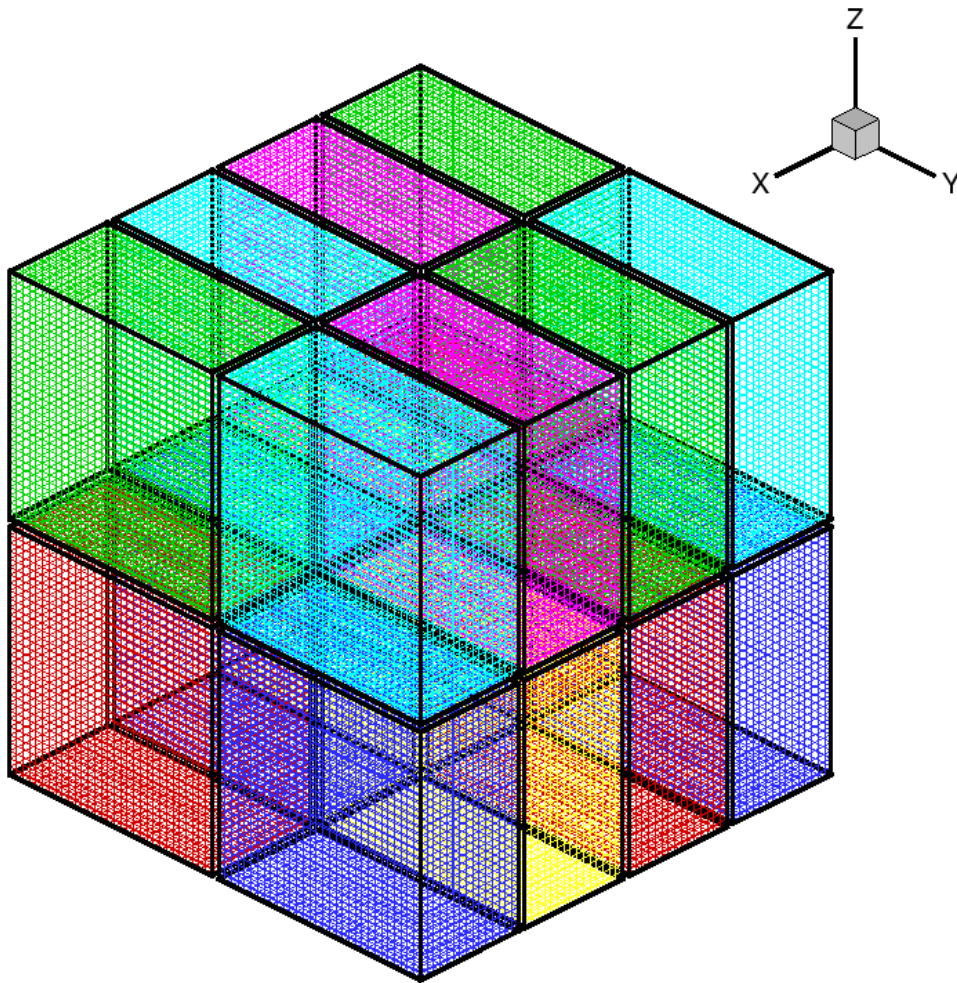
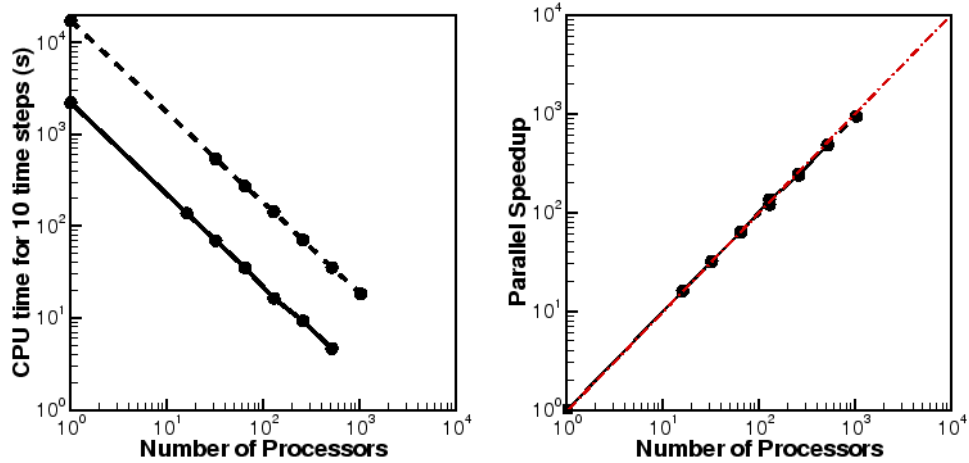
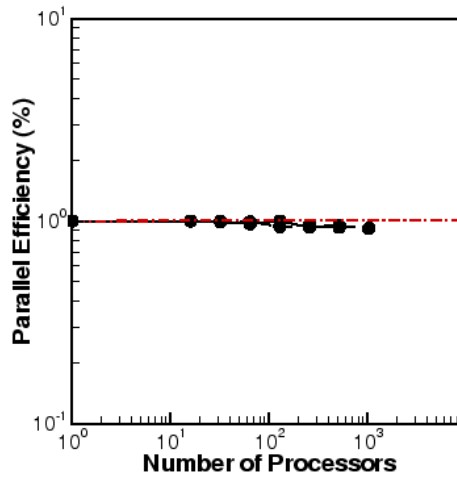


Fig. 7. Mesh and domain decomposition for $64 \times 64 \times 64$ grid with a $4 \times 2 \times 2$ processor configuration



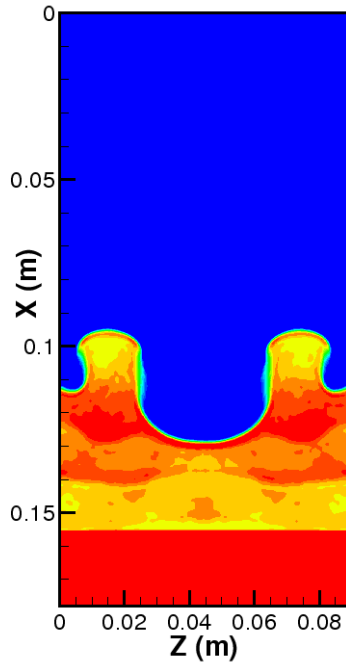
(a)

(b)

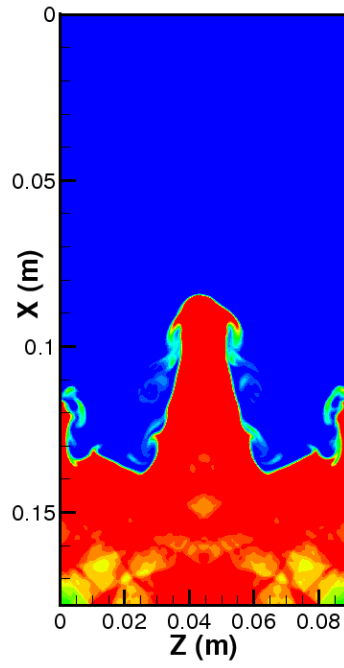


(c)

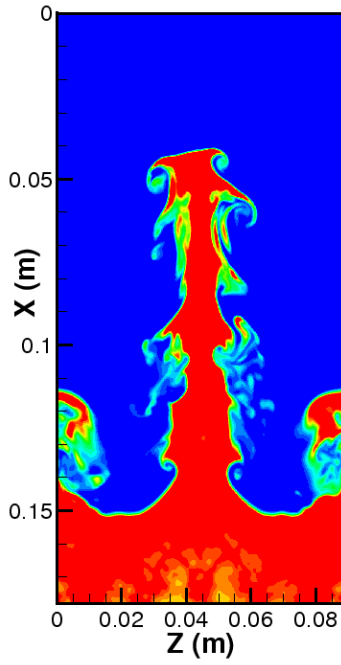
Fig. 8. Parallel scaling analysis for the solution of the Euler hydrodynamics system (Eqns. (3) - (5)) on two different problem sizes: (a) CPU time for 10 time steps, (b) Speedup, and (c) Efficiency; Solid line with symbols: 128^3 ; Dashed line with symbols: 256^3 . The red dashed line indicates perfect or ideal values.



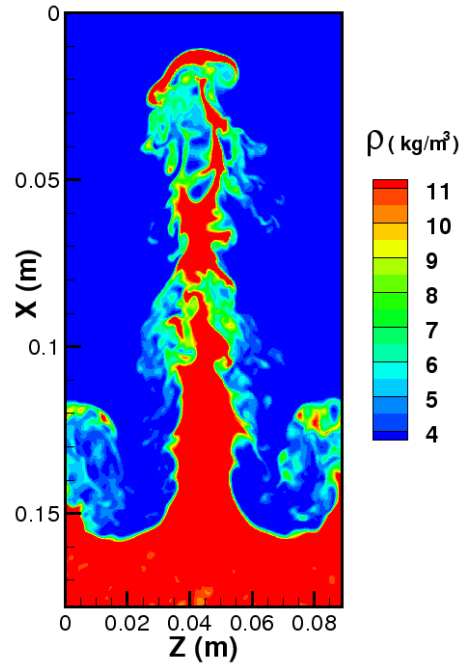
(a)



(b)

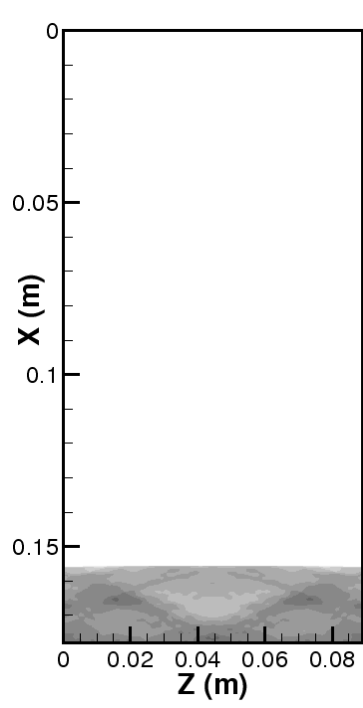


(c)

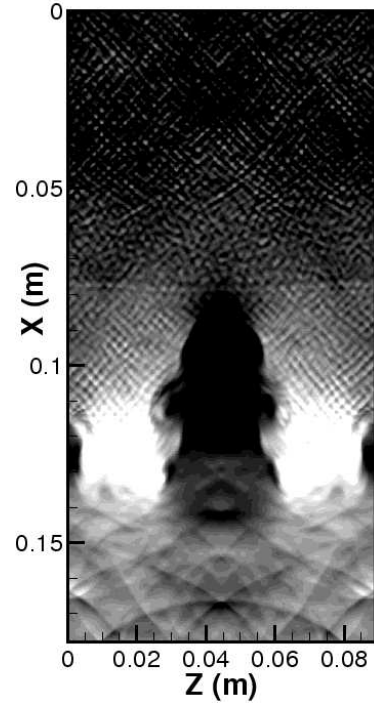


(d)

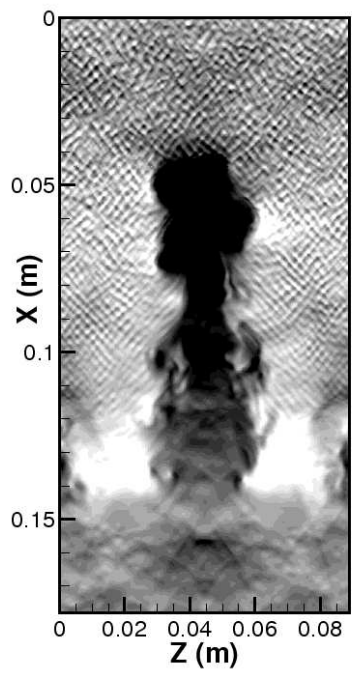
Fig. 9. Instantaneous contours of density across centerline Y direction ($Y = 0$ at (a) $t = 1$ ms, (b) $t = 2$ ms (c) $t = 3$ ms and (d) $t = 4$ ms.



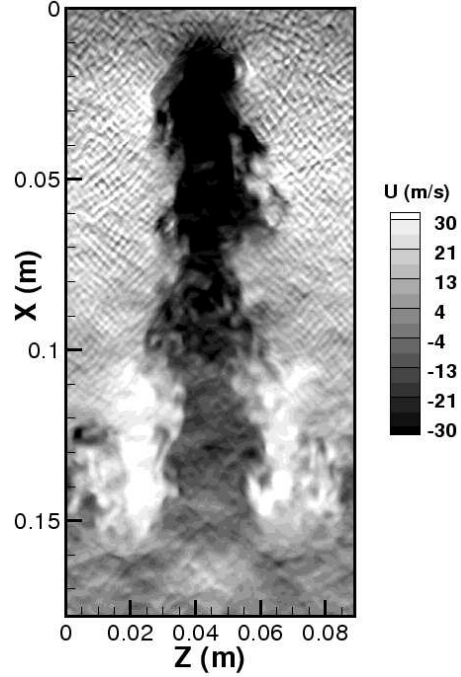
(a)



(b)



(c)



(d)

Fig. 10. Instantaneous contours of X -velocity across centerline Y direction ($Y = 0$) at (a) $t = 1$ ms, (b) $t = 2$ ms (c) $t = 3$ ms and (d) $t = 4$ ms.

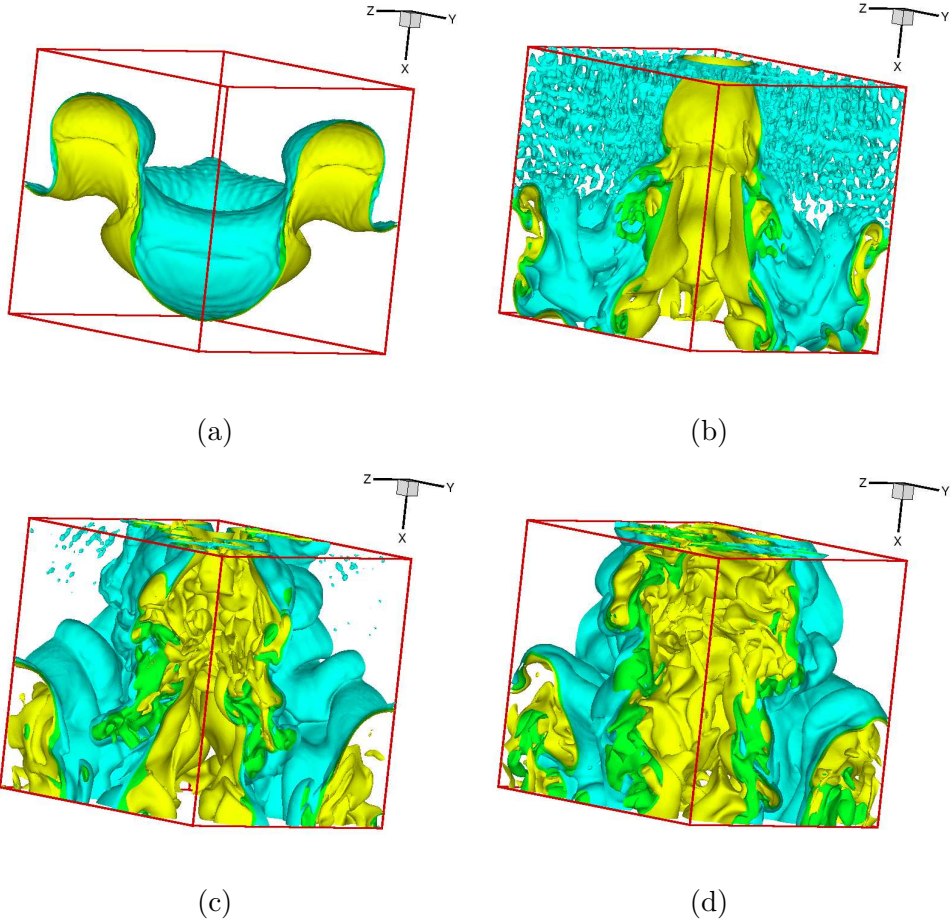
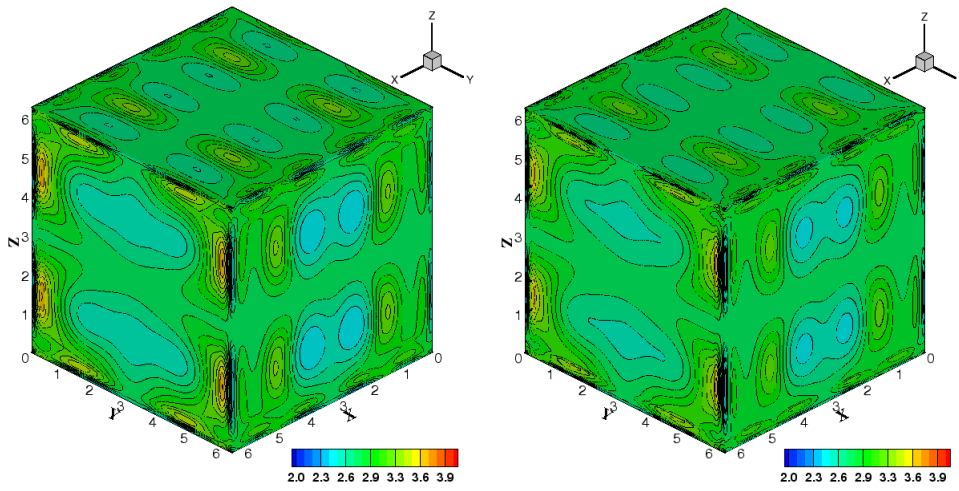


Fig. 11. Instantaneous isosurfaces of density ($C = 7$ and $C = 9$) on a sub-domain of size $4.5 \times 4.5 \times 4.5 \text{ cm}^3$ (a) $t = 1 \text{ ms}$, (b) $t = 2 \text{ ms}$ (c) $t = 3 \text{ ms}$ and (d) $t = 4 \text{ ms}$.



(a)

(b)

Fig. 12. Instantaneous contours of density across X , Y and Z direction-centerlines ($= \pi$) at $t = 0.2$ for two different grid sizes 128^3 (left) and 256^3 (right).

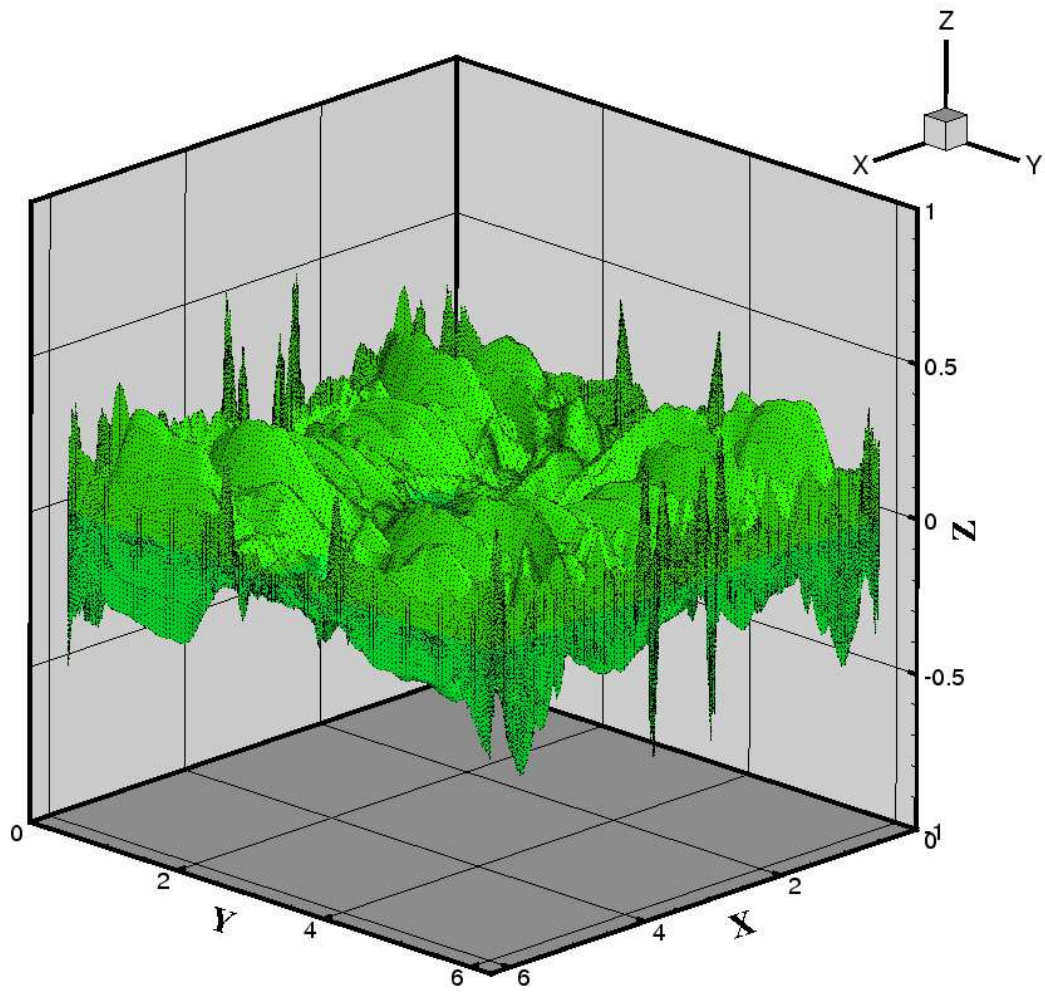


Fig. 13. Instantaneous surface plot of the divergence of the magnetic field ($\nabla \cdot \mathbf{B}$) on all the Z -surfaces at $t = 0.5$ for the solution of the Orszag-Tang system.

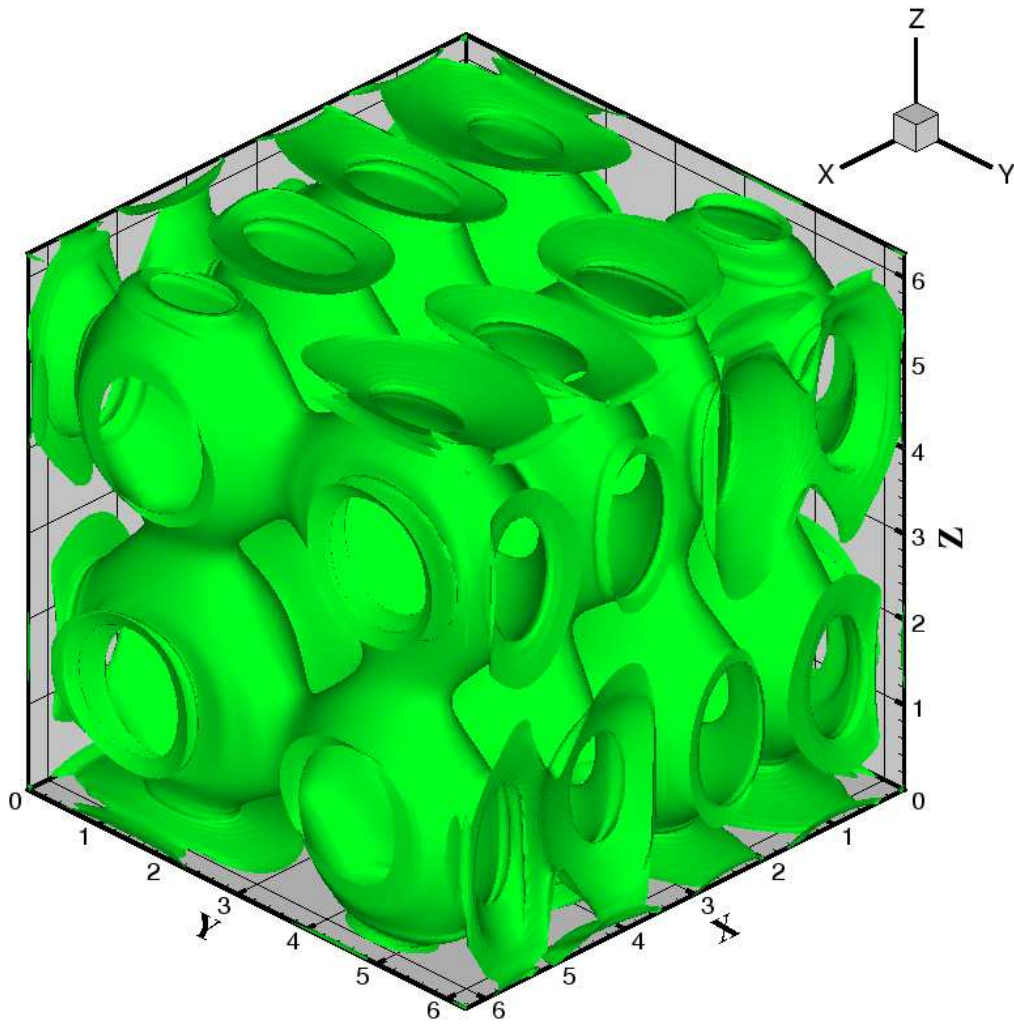
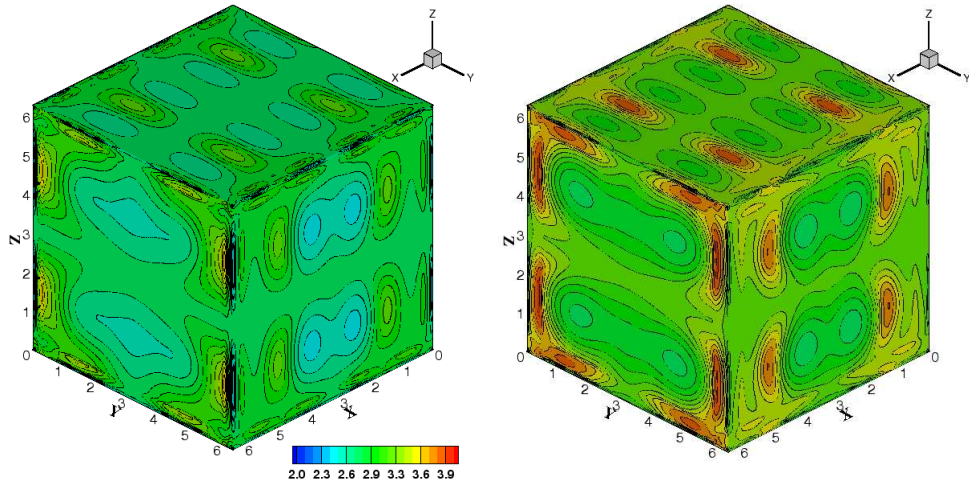
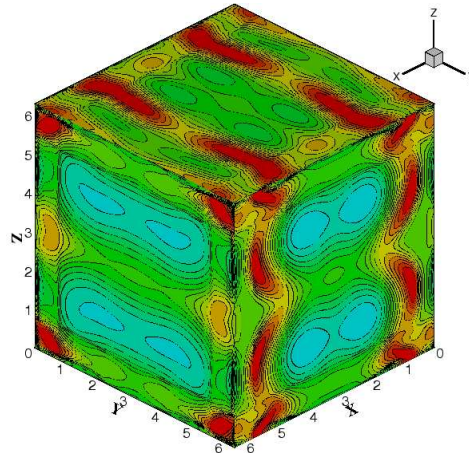


Fig. 14. Isosurface of the density at a value $\rho_C = 3.0$ at $t = 0.2$.



(a)

(b)



(c)

Fig. 15. Instantaneous contours of density across X , Y and Z direction-centerlines ($= \pi$) at (a) $t = 0.2$, (b) $t = 0.4$ and (c) $t = 0.8$; (Grid: 256^3).

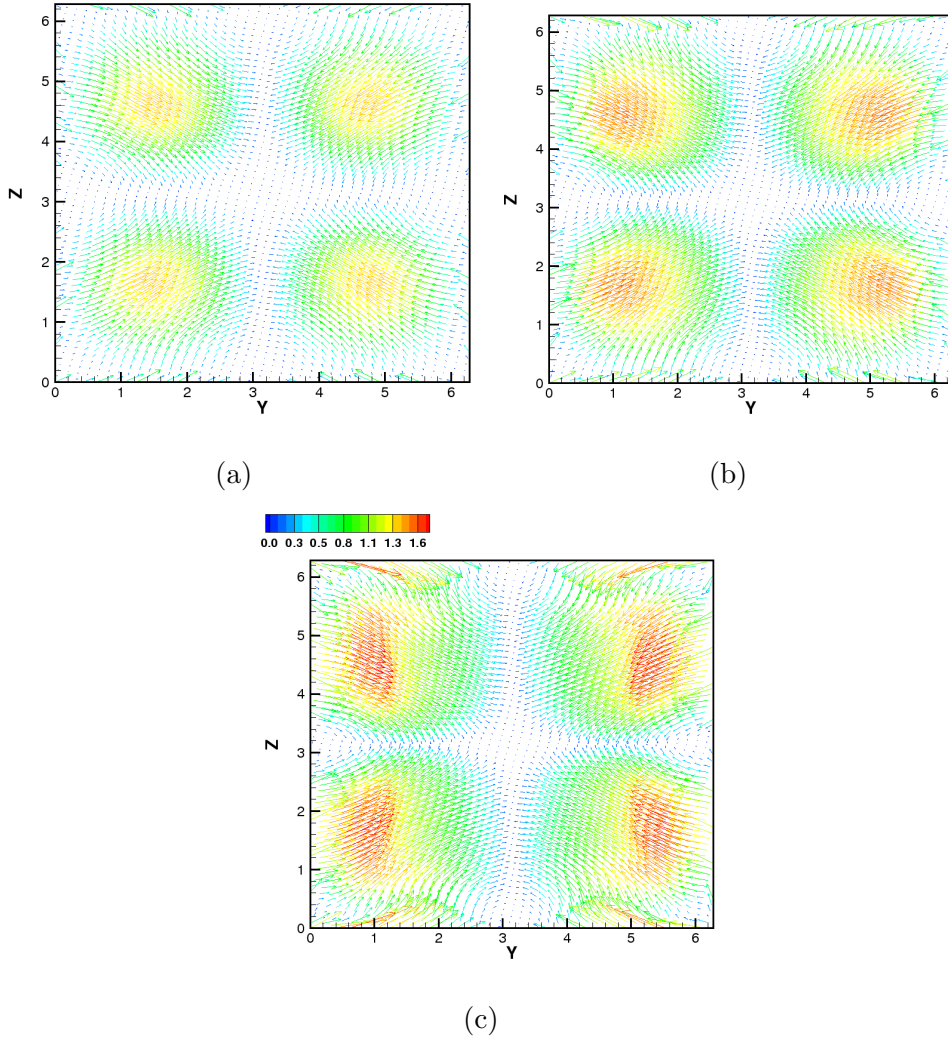


Fig. 16. Instantaneous slices across the X -direction centerline ($= \pi$) showing vectors of the $2D$ magnetic field (B_y, B_z) colored by the magnitude of the magnetic field at (a) $t = 0.2$, (b) $t = 0.4$ and (c) $t = 0.8$; (Grid: 256^3).